remote sensing

MDPI

Article

Analysis of Urbanization-Induced Land Subsidence in the City of Recife (Brazil) Using Persistent Scatterer SAR Interferometry

Wendson de Oliveira Souza [1], Luis Gustavo de Moura Reis [2], Jaime Joaquim da Silva Pereira Cabral [3,4], Antonio Miguel Ruiz-Armenteros [5,6,7,*], Roberto Quental Coutinho [3], Admilson da Penha Pacheco [3] and Wilson Ramos Aragão Junior [3]

1 Department of Transports and Geomatics, Center for Technology, Federal University of Piauí (UFPI), Teresina 64049-550, Brazil; wendsonsouza@ufpi.edu.br
2 Acquaprojetos Hydrology and Drainage Consulting, Avenue Carlos Gomes, Porto Alegre 90480-002, Brazil; luisgustavo@acquaprojetos.com.br
3 Center for Technology and Geosciences, Federal University of Pernambuco (UFPE), Recife 50670-901, Brazil; jaime.cabral@ufpe.br (J.J.d.S.P.C.); roberto.coutinho@ufpe.br (R.Q.C.); admilson.pacheco@ufpe.br (A.d.P.P.); wilson.ramos@ufpe.br (W.R.A.J.)
4 Department of Civil Engineering, Polytechnic School, University of Pernambuco (UPE), Recife 50720-001, Brazil
5 Department of Cartographic, Geodetic and Photogrammetry Engineering, University of Jaén, Campus Las Lagunillas s/n, 23071 Jaén, Spain
6 Microgeodesia Jaén Research Group (PAIDI RNM-282), University of Jaén, Campus Las Lagunillas s/n, 23071 Jaén, Spain
7 Center for Advanced Studies on Earth Sciences, Energy and Environment CEACTEMA, University of Jaén, Campus Las Lagunillas s/n, 23071 Jaén, Spain
* Correspondence: amruiz@ujaen.es

check for updates

Citation: Souza, W.d.O.; de Moura Reis, L.G.; da Silva Pereira Cabral, J.J.; Ruiz-Armenteros, A.M.; Quental Coutinho, R.; da Penha Pacheco, A.; Ramos Aragão Junior, W. Analysis of Urbanization-Induced Land Subsidence in the City of Recife (Brazil) Using Persistent Scatterer SAR Interferometry. *Remote Sens.* **2024**, *16*, 2592. https://doi.org/10.3390/rs16142592

Academic Editors: Fabio Rocca and Deodato Tapete

Received: 17 April 2024
Revised: 5 July 2024
Accepted: 12 July 2024
Published: 15 July 2024

Abstract: The article addresses anthropogenic and geological conditions related to the development of soil subsidence in the western zone of Recife (Brazil). Over the past 50 years, human activity has intensified in areas previously affected by soft soils (clay, silt, and sandstone) resulting in subsidence due to additional loads (landfills and constructions). The duration of the settlement process can be significantly influenced by the specific characteristics of the soil composition and geological conditions of the location. This work presents, for the first time, accurate InSAR time series maps that describe the spatial pattern and temporal evolution of the settlement, as well as the correlation with the geological profile, and validation with Global Navigation Satellite System (GNSS) data. Persistent Scatterer Interferometry (PS-InSAR) was employed in the analysis of Single Look Complex (SLC) images generated by 100 ascending COSMO-SkyMed (CSK) and 65 PAZ (32 ascending, and 33 descending) from the X-band, along with 135 descending Sentinel-1 (S1) acquisitions from the C-band. These data were acquired over the period from 2011 to 2023. The occurrence of subsidence was identified in several locations within the western region, with the most significant displacement rates observed in the northern, central, and southern areas. In the northern region, the displacement rates were estimated to be approximately −20 mm/year, with the Várzea and Caxangá neighborhoods exhibiting the highest rates. In the central region, the displacement rates were estimated to be approximately −15 mm/year, with the Engenho do Meio, Cordeiro, Torrões, and San Martin neighborhoods exhibiting the highest rates. Finally, in the southern region, the displacement rates were estimated to be up to −25 mm/year, with the Caçote, Ibura, and Ipsep neighborhoods exhibiting the highest rates. Additionally, east–west movements were observed, with velocities reaching up to −7 mm/year toward the west. These movements are related to the lowering of the land. The study highlights that anthropogenic effects in the western zone of Recife contribute to the region's vulnerability to soil subsidence.

Keywords: land subsidence; urbanization; PS-InSAR; multi-sensors; time series; monitoring

1. Introduction

Land subsidence is a geological and environmental hazard that results in the ground sinking. It can occur in natural or urbanized areas and significantly impacts the environment, infrastructure, and urban development [1,2]. The process of subsidence can take a long time and can reach notable sink rates and cumulative values [2,3].

This phenomenon is frequently the result of high-impact anthropogenic activities [4], which can lead to a reduction in the subsoil's bearing capacity or the settlement of its compressible layers. Examples of such activities include the extraction of oil, gas, and minerals [5] as well as the overexploitation of groundwater resources [6–10]. Additionally, the construction of new buildings in urbanized areas can place further loads on the soil, contributing to the phenomenon of soil subsidence. Cases of soil subsidence due to urban development have been reported worldwide, including in Roma [11], Tuscany [12], Shanghai [13], Beijing [14], Uppsala [15], and Riad [16].

Recife, the capital of the Brazilian state of Pernambuco, is one of the oldest cities in the country, with a history that can be traced back to the 16th century. The city's population is estimated to be approximately 3.7 million in the metropolitan area [17], which encompasses an extensive coastal plain. Recife's urbanization has primarily occurred in the estuarine region of the Capibaribe River, where land has been reclaimed from mangrove forests, streams, and wetlands. As is the case with developing countries, the rapid urbanization that has occurred over the past 50 years has had several consequences, with the most notable being the reduction in groundwater recharge and over-exploitation in the southern region of the city [18].

In Recife, the consequences of groundwater over-exploitation have been extensively investigated, particularly the salinization of saltwater intrusion in regional aquifers (e.g., Montenegro et al. [19]), and its effects on soil subsidence have become a concern of the technical and scientific community. In this context, the investigations conducted by Santos [20] and Luna et al. [21,22], who employed geodetic techniques (leveling, GNSS) to detect vertical displacements, are noteworthy.

Further investigation is required to elucidate the causes of soil subsidence in Recife, particularly in light of the growing availability of SAR data. Recently, Bedini [23] employed Persistent Scatterer Interferometry (PS-InSAR) analysis over 68 Sentinel-1 time series imagery datasets spanning 2.5 years from April 2017 to September 2019 to study this region. This work represents a preliminary investigation of the phenomenon of ground subsidence using SAR data. The main findings of this study are as follows. (1) The subsiding area, which is situated in the West Zone of Recife (WZR), is the result of the broadening of neighborhoods in Afogados, Torrões, and Cordeiro. The subsidence rate is up to −15 mm/year. (2) Smaller areas, which are located in several localities, have a subsidence rate of up to −25 mm/year. These areas have experienced subsidence due to the construction of new buildings in the last decade.

Further research is required to quantify and monitor soil subsidence in other regions of the Recife Metropolitan Region (RMR), particularly the WZR, which has been subjected to recent urbanization and the construction of numerous buildings. This is in addition to the southern areas, which have experienced groundwater overexploitation and subsequent subsidence.

This study aimed to expand the scope of soil subsidence analysis in the West Zone of Recife through the use of high-spatial-resolution SAR images, which were supported by geotechnical and GNSS data. For the first time, the study provides accurate InSAR time series maps that describe the spatial pattern and temporal evolution of the displacements, as well as the correlation with the geotechnical profile and validation with GNSS data. The mapping of detailed surface displacements enabled the identification of locations with the potential for ground subsidence, irrespective of field observations or previous studies.

The ground subsidence of the WZR was evaluated using the PS-InSAR technique on the SLC images dataset, which consisted of 100 ascending COSMO-SkyMed SAR images, 65 PAZ SAR images (32 ascending and 33 descending) of the X-band, and 135 Sentinel-1

SAR images of the C-band, acquired between July 2011 and March 2023 (11.7 years). The study confirmed the active presence of several sinking sites in the WZR, with the main displacement rates observed in neighborhoods in the central parts (Torrões, Engenho do Meio, Curado, San Martin, Cordeiro, Prado, and Afogados) and south (Caçote, Ibura, and Ipsep), as well as in the north (Caxangá, and Várzea). The displacement rates were found to be consistent with the thickness of compressible sedimentary layers, including clay, silt, and sandstone.

2. Study Area

2.1. Geographic and Topographic Setting

The study focuses on the WZR, the capital of the State of Pernambuco, located in northeast Brazil. Recife is the fourth most densely populated metropolitan area in the country, with an area of approximately 218 km^2 and an estimated population of 1.66 million inhabitants [24]. Recife is situated on the estuarine region of the Capibaribe River (Figure 1) and is crossed by the Beberibe and Tejipió's Rivers. It is also known as an archipelago city [25] or commonly as "Brazilian Venice". The sea level elevation varies from around 5 m in the city's central area, which is characterized by flat topography, to more than 100 m in high-rugged hills. Nevertheless, over half of the territory is situated at altitudes below 20 m.

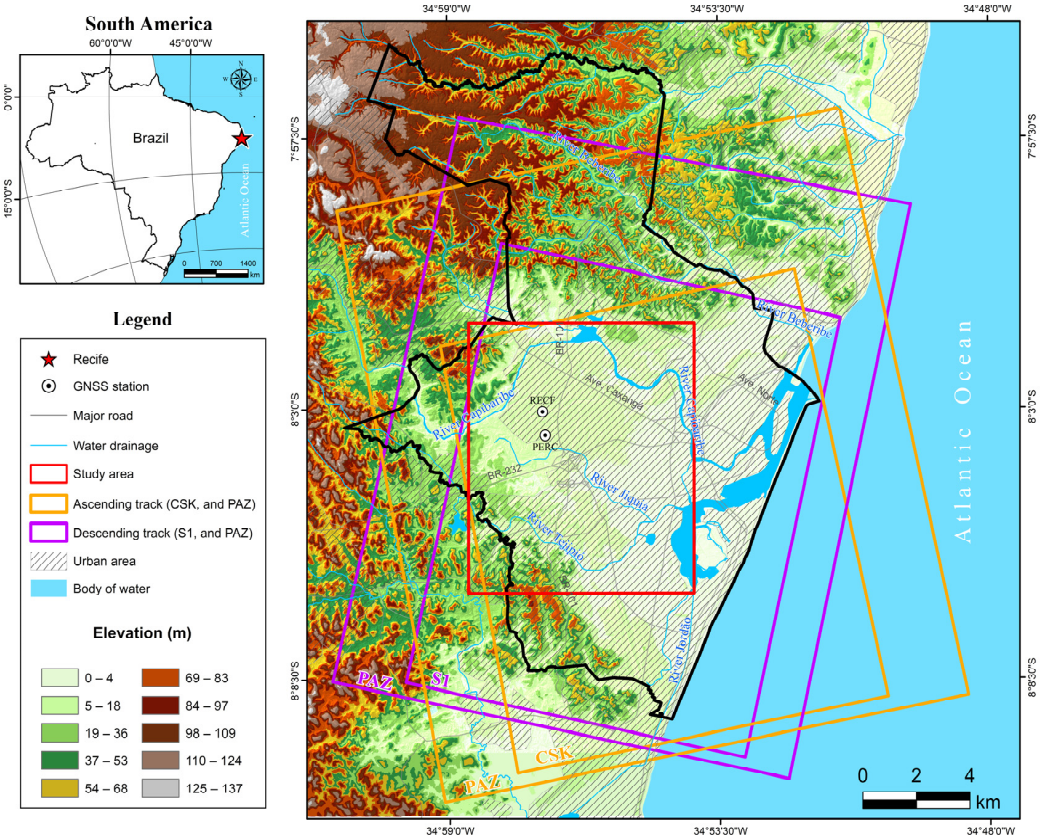

Figure 1. Location of the study area with elevation map.

The WZR region is characterized by a predominantly flat topography, with elevations below 10 m in the central region and below 100 m in the northern and southern extremities. The region is traversed by three rivers: Capibaribe, Tejipió, and Jiquiá. It encompasses approximately 48.92% of Recife's urban area and is home to an estimated population of 830,000 individuals. The location is readily accessible from the interior of the state via the BR-232 highway and from the north–south axis via the BR-101 highway.

2.2. Geological and Geomorphological Features

The WZR's geological setting is predominantly situated in a coastal marine environment, comprising sandy sediments, river lagoons, and mangroves (Figure 2). The sandy sediments are intermixed with clayey layers and organic matter (peat), which rest on top of older Quaternary sediments [26]. In several locations, a layer of silty-sandy and clay-sandy grain size with a soft consistency is found just below the sandstone, along with a sandstone package and resistant material from 15 to 30 m deep. Silty clay deposits with soft to very soft consistency, high compressibility, and a thickness greater than 25 m are common. The mangrove sediments are composed of clay, silt, fine sand, and a considerable quantity of organic matter that accumulates in peat deposits in estuarine environments situated in the final courses of rivers.

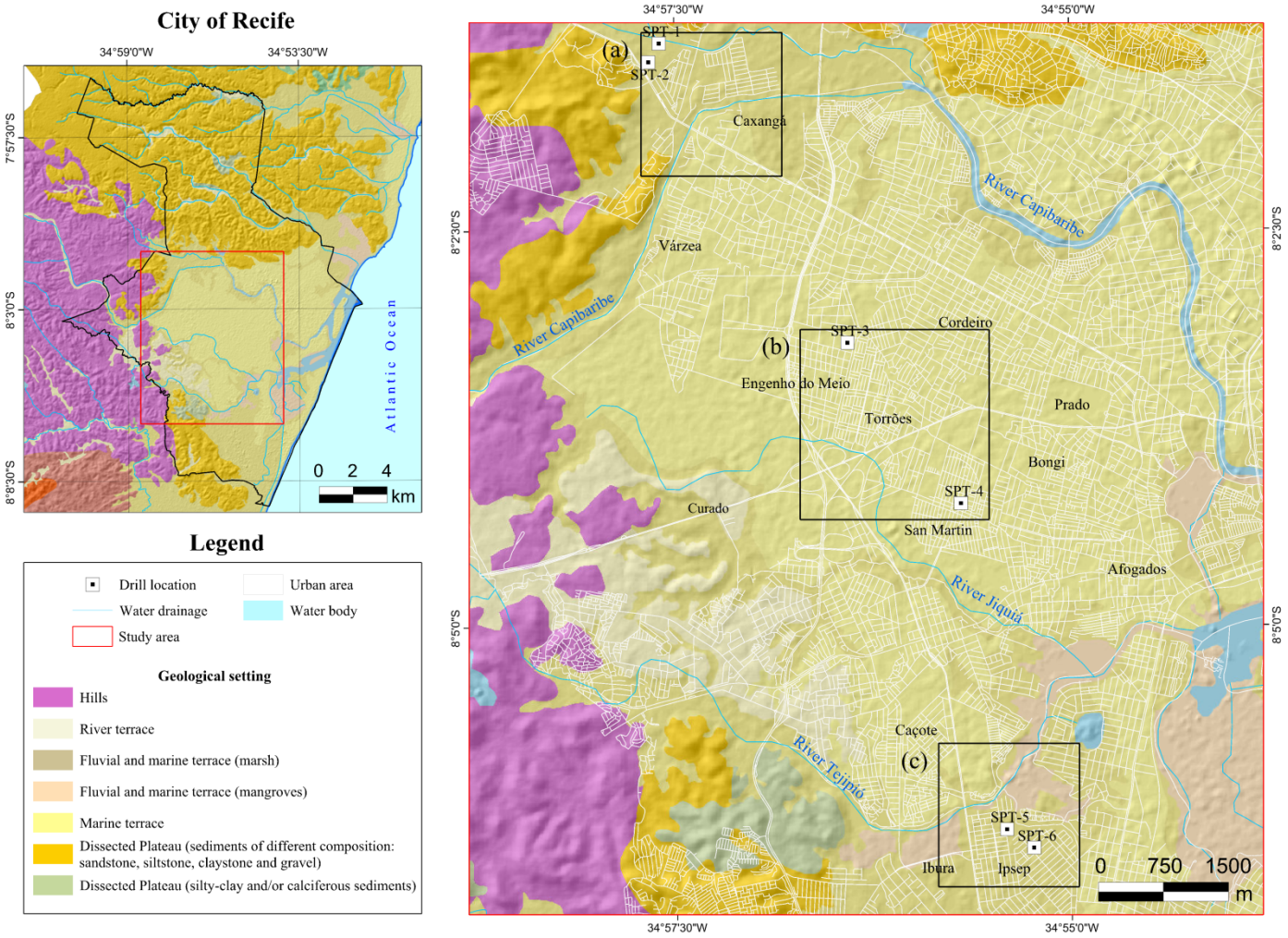

Figure 2. Geological environment of the Recife. Base map © Geodiversity map of the metropolitan region of Recife-PE © Geological Survey of Brazil (CPRM). Black rectangles (**a**–**c**) represent the mapped areas in Figure 3.

2.3. Urban Development

The process of occupation and urban expansion of Recife commenced on relatively flat terrain in the 17th century, a period during which Recife was under Dutch rule (1630–1654). From that time until the present century (21st), the city of Recife underwent profound transformations in its physiognomy and structure. These transformations were largely the result of the reclamation of land from mangroves, streams, and wetlands for urbanization purposes. In chronological order, the city's construction dynamics originated from the center (port activity) to the north (hills), south (beaches), and, finally, the west (interior)

regions. In this regard, the western zone is the most recently urbanized due to its relatively late occupation process. The city's central area was among the most significantly impacted. A landfill of approximately 190 ha with an average depth of 2.50 m was in operation until the beginning of the 20th century.

During the 20th century, Recife's urban development continued by expanding into new areas of plain waters and geographical features in the north, south, and west (as shown in Figure 3). The city experienced a period of rapid growth during this period, which was achieved through the occupation of hills, the embankment of river beds, and the expansion over flooded areas. The unplanned urbanization of Recife resulted in the loss of numerous secondary watercourses and the confinement of the river floodplains, leading to significant changes. In the middle of the century, the WZR underwent significant transformations including the construction of government institutions (UFPE, SUDENE, and IFPE), the implementation of industrial areas, and the expansion of highways (BR-101 and BR-232) (Figure 3). These actions contributed to the accelerated urban growth in the WZR, particularly the neighborhoods of Várzea, Curado, Engenho do Meio, Iputinga, Caxangá, Cordeiro, and Torrões, which placed greater strain on the city. Among these, it is notable that the urban drainage system is overloaded and insufficient, with numerous flooding points, particularly in areas of low elevation [18,27].

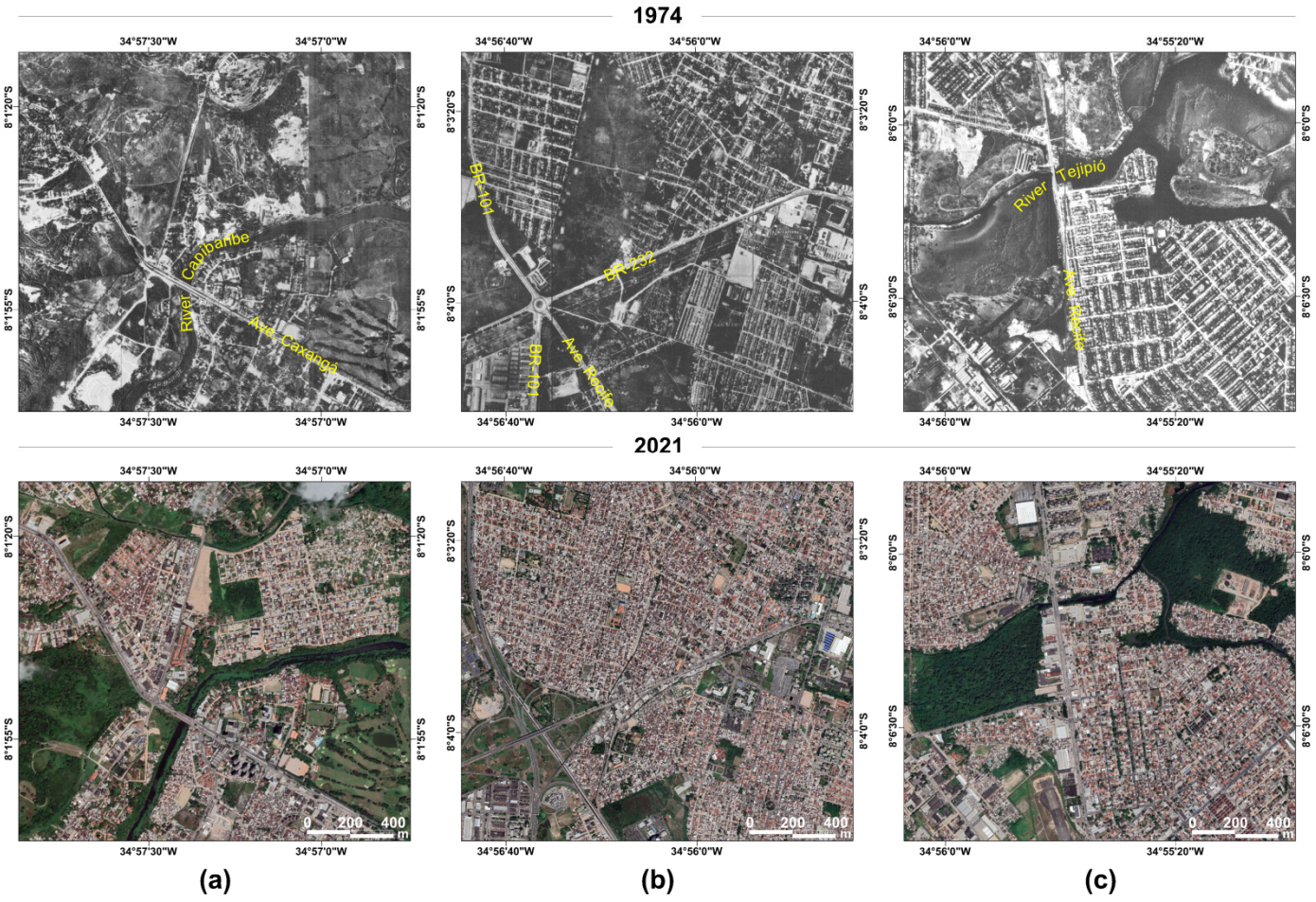

Figure 3. Evolution of urbanization from 1974 [28] to 2021 [29]. West Zone of Recife (WZR) areas: (**a**) Várzea and Caxangá neighborhoods, (**b**) Engenho do Meio, Cordeiro, Torrões, and San Martin neighborhoods, and (**c**) Caçote, Ibura, and Ipsep neighborhoods.

3. Data and Methods

3.1. SAR Dataset

The analysis of ground subsidence detection in WZR employed Single Look Complex (SLC) SAR images from the COSMO-SkyMed, Sentinel-1, and PAZ satellites.

The multi-temporal SAR datasets (Table 1) employed in the study spanned the period from 2011 to 2023. As illustrated in Figure 4, the time series datasets consisted of the following SLC SAR images: 100 ascending COSMO-SkyMed (CSK) images from July 2011 to December 2019, 135 descending Sentinel-1 (S1) images from September 2016 to April 2021, and 65 PAZ (32 Ascending and 33 Descending) images from October 2019 to March 2023.

Table 1. SAR dataset specifications.

Parameters	COSMO-SkyMed	Sentinel-1	PAZ
Wavelength	3.4 cm (X-band)	5.6 cm (C-band)	3.4 cm (X-band)
Sensor mode	StripMap HIMAGE	IW1	StripMap
Polarization	Single (HH)	Single (VV)	Single (HH)
Pass direction	Ascending	Descending	Ascending and Descending
Spatial resolution	2.6 m × 2.6 m	2.3 m × 14.1 m	1.76 m × 3.01 m
Incidence angle	19.93°–20.11°	37°–39°	38° (asc)–22° (desc)
Swath width	40 km	240 km × 170 km	30 km × 50 km
Temporal resolution	30 days	12 days	33 days

Note: spatial resolution is range × azimuth and IW1 is Interferometric Wide Swath with Sub-swath 1.

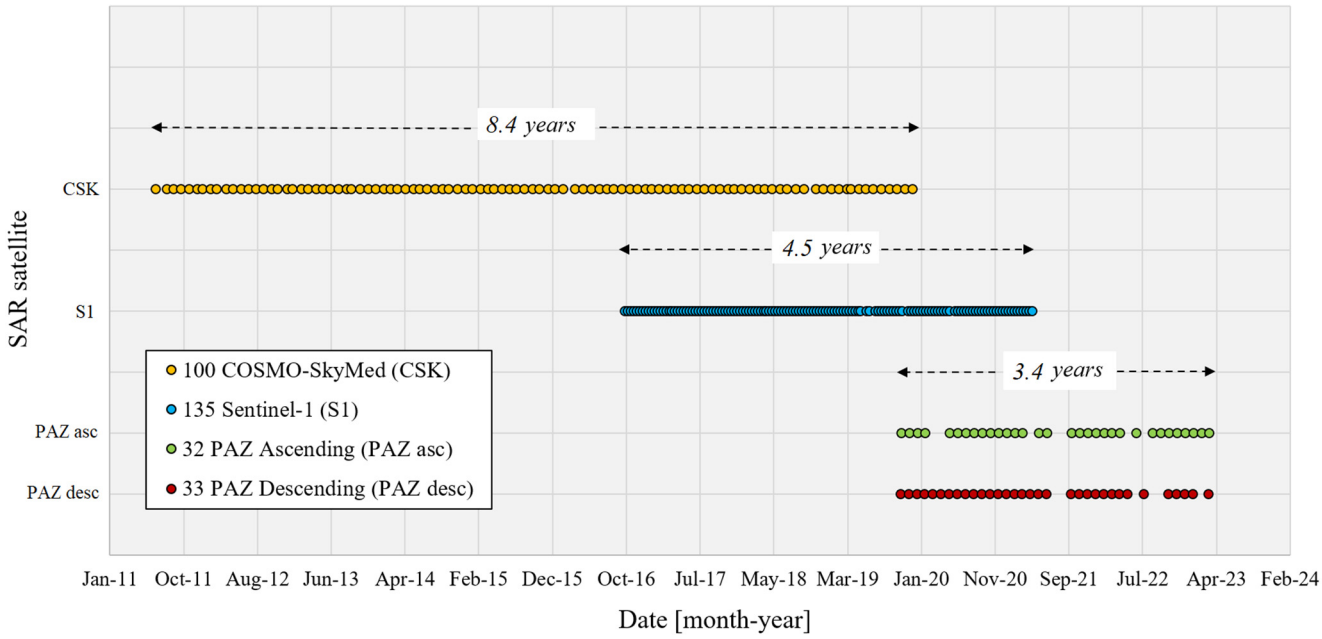

Figure 4. Temporal coverage of SAR images.

3.2. PS-InSAR Processing

The PS-InSAR technique [30] was employed to identify deformation in the WZR. The method exploits phase information to measure the ground displacement by selecting a set of measuring points (or targets) known as Persistent Scatterers (PS). PSs are characterized by stable radiometric behavior over time. They are typically natural structures (e.g., rocky outcrops or exposed soil) or artificial structures (e.g., buildings and infrastructures) [31]. The PS-InSAR application has proven effective in identifying PS pixels in urban and non-urban areas that are subject to permanent or periodic deformation [32].

PS-InSAR represents an advancement of the Differential Interferometric Synthetic Aperture Radar (DInSAR) technique, which employs the integration of multiple SAR

images acquired over the same area [31]. The application of DInSAR is constrained by temporal and geometric decorrelation. Multitemporal InSAR approach (MT-InSAR) methods are useful to overcome these limitations. This study employed the PS-InSAR technique in conjunction with the classic MT-InSAR processing approach [33], which involved the estimation of linear deformation over time to generate a displacement time series. The selection of potential PS candidates (PSC) was based on different parameters including the amplitude stability index (ASI), spatial coherence, and reflectivity. The processing workflow is depicted in Figure 5.

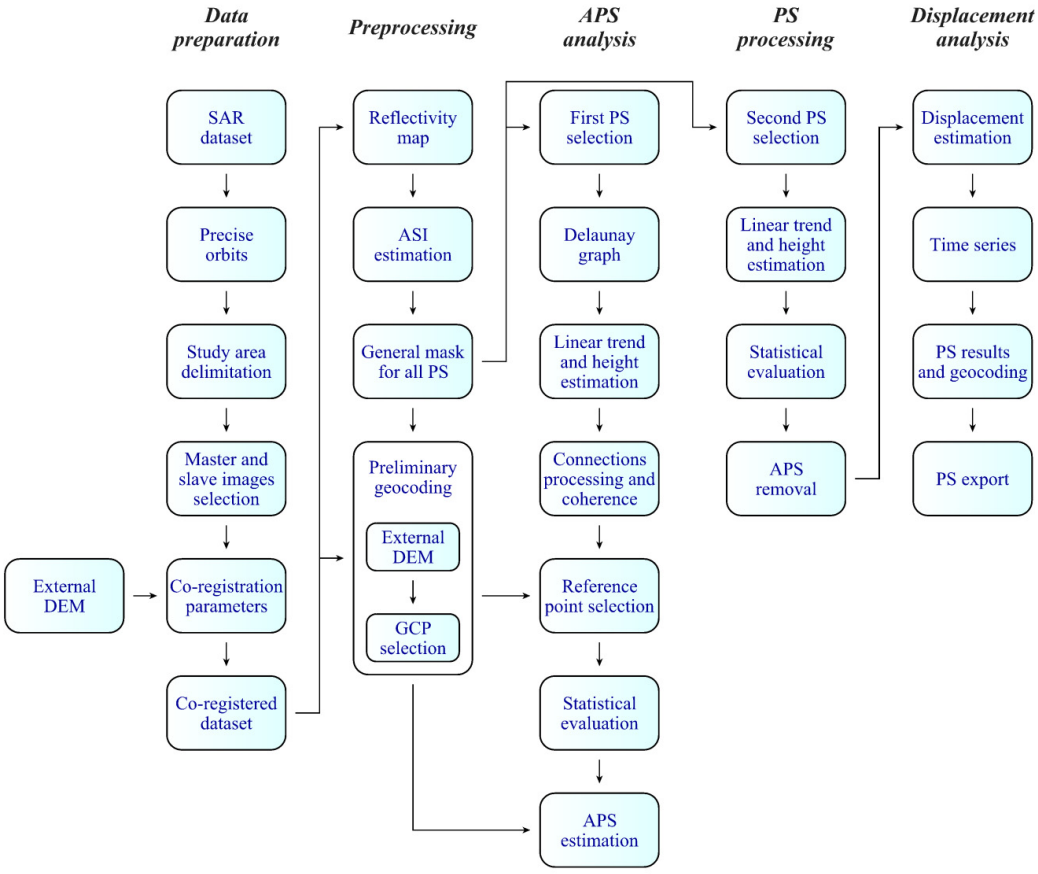

Figure 5. PS-InSAR processing workflow.

In Figure 5, the PS analysis was conducted using the SARPROZ software [34]. The utilization of this software permitted the processing of data from different SAR sensors. For Sentinel-1 images, the software automatically downloaded Precise Orbit Ephemerides (POE). For COSMO-SkyMed and PAZ images, precise orbits were employed that were specific to the respective scenes. The Digital Elevation Model (DEM) with a spatial resolution of 1 m provided by the Pernambucana Water and Climate Agency (APAC) was employed to flatten the interferograms.

The N–1 interferograms were generated by selecting a single SAR image as the reference N (master image). SARPROZ automatically selected the master SLC image to minimize the effects of decorrelation of normal and temporal baselines [35]. Figure 6 depicts the relationship between the slave images and interferograms in the normal and temporal baselines in relation to the master image. The dates of the master images are as follows: 17 January 2016 (COSMO-SkyMed), 21 October 2018 (Sentinel-1), 9 June 2021 (PAZ asc), and 4 May 2021 (PAZ desc).

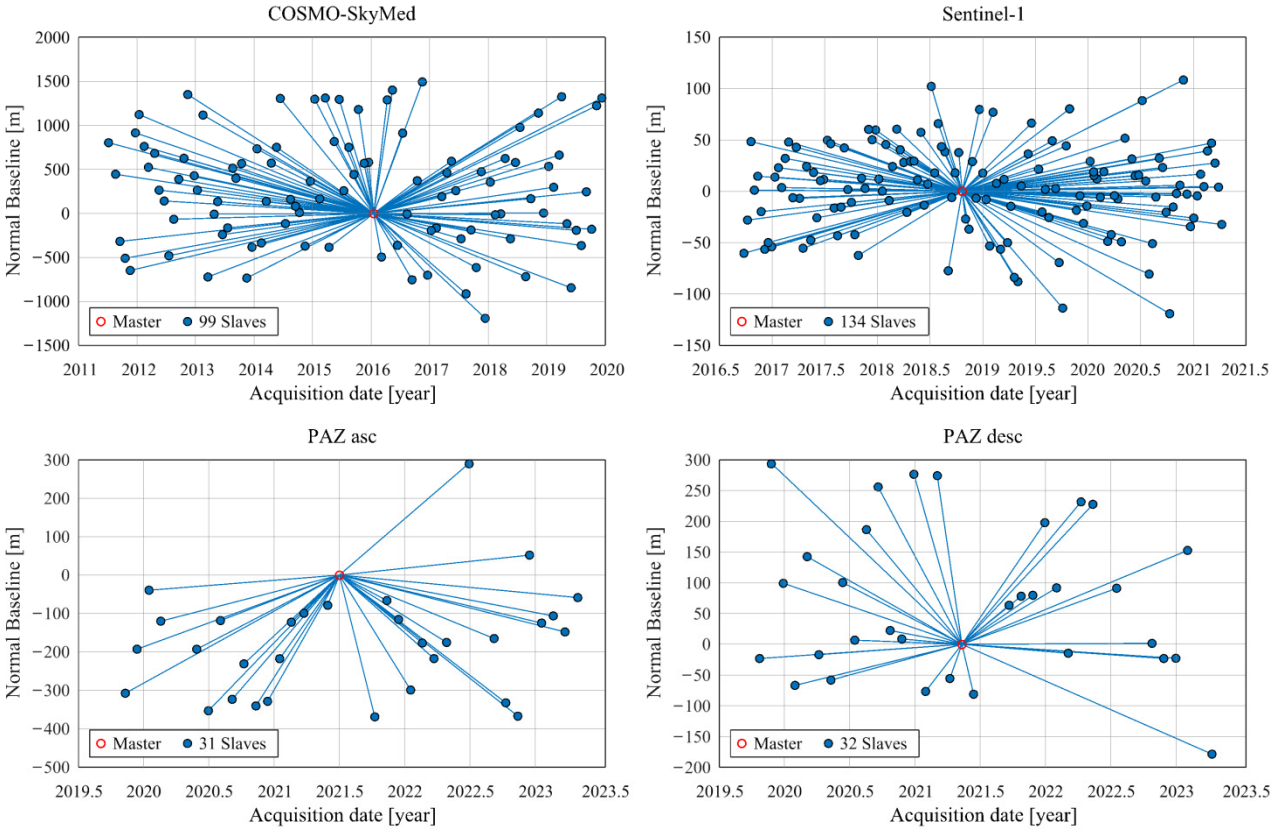

Figure 6. Interferogram formation for the SAR datasets with interferometric pairs between the master and slaves.

The utilization of a master SLC image served as a reference in the co-registration of radar scenes with precise orbit applications. To eliminate the topographic phase component, an external digital elevation model (DEM) was employed. Additionally, the SAR datasets were geocoded using a high-reflection Ground Control Point (GCP) identified on a reflectivity map generated by the software. The removal of the Atmospheric Phase Screen (APS) component was performed based on the selection of PSCs points with an ASI value greater than 0.8. The reference point was chosen manually in a stable area, with no record of deformation.

The final analyses involved the selection of PSCs pixels with an ASI value greater than 0.6 and temporal coherence greater than 0.7. The data were geocoded and exported from the software and then transformed into PS points. The products of the PS-InSAR analysis included the Line-Of-Sight (LOS) velocity and deformation time series.

Furthermore, the availability of ascending and descending geometries of PAZ images permitted an investigation of the direction of ground motion and the calculation of the components of the vertical zenith-nadir (d_V) and horizontal east–west (E–W) (d_H) displacements as follows [36] (Equation (1)):

$$\begin{bmatrix} d_H \\ d_V \end{bmatrix} = \begin{bmatrix} \sin\theta_{asc}\cos\phi_{asc} & \cos\theta_{asc} \\ \sin\theta_{desc}\cos\phi_{aesc} & \cos\theta_{desc} \end{bmatrix}^{-1} \begin{bmatrix} d_{asc} \\ d_{desc} \end{bmatrix} \quad (1)$$

where d_{asc} and d_{desc} represent the LOS deformation for the ascending and descending datasets, respectively. ϕ_{asc} and ϕ_{desc} are the horizontal angles of the LOS directions measured from the south in a clockwise direction; θ_{asc} and θ_{desc} are the satellite beam angles for the ascending and descending directions. North–south horizontal displacements projected in the LOS (line-of-sight) are considered negligible and are mapped into the other components of the estimated displacements.

3.3. Land Cover Data

To identify changes in land cover that occurred in the study area, vector data of plots were utilized with information from the year of its implementation made available by the City of Recife's administration [37]. The analysis entailed classifying built-up areas over time to infer the age of changes resulting from urbanization. To ascertain the extent of urban expansion in the west zone, population data from Recife [24] were employed to cross-relate the observed trends.

3.4. Geotechnical Profiles

To analyze and discuss the research findings in the context of the local geological and geotechnical conditions, in situ geotechnical profiles were analyzed. The objective was to establish a correlation between the verified PS-InSAR displacements and the characteristics of the subsoil layers. Six borehole profiles were selected from a standardized research project database maintained by the Group of Geotechnical Engineering of Slopes, Plains, and Disasters (GEGEP) at the Federal University of Pernambuco (UFPE) [38,39]. These profiles are situated over the plains of Recife (as shown in Figure 2).

3.5. GNSS Data

Information from the Brazilian Network for Continuous Monitoring of the GNSS Systems (RBMC), stations RECF (Recife) [40], and PERC (Pernambuco Recife) [41] was employed to evaluate the vertical and horizontal displacement of WZR and validate the PS-InSAR results. The stations (Figure 1) were equipped with high-performance GNSS receivers to obtain geodetic coordinates and their velocities referred to SIRGAS2000 (Geocentric Reference System for the Americas, based on ITRF2000) at epoch 2010.0 [42]. The geodetic network is part of the Brazilian Geodetic System (SGB) maintained by the Brazilian Institute of Geography and Statistics (IBGE). IBGE is responsible for implementing, defining, and maintaining geodetic structures in the country.

As a consequence of the displacement of the South American tectonic plate, which affected the RECF and PERC stations, the SARI software [43] was employed to remove the plate velocity from the north, east, and vertical components. Subsequently, the residual velocity of the actual ground motion, where the stations are located, was projected onto the LOS direction, as described in Hanssen [44]. This approach enabled the results of the stations' motion to be validated.

4. Results

4.1. PS-InSAR Deformation Maps and Time Series

PS-InSAR monitoring is presented in maps of mean deformation rate (Figure 7) and displacement time series for the 11.7-year time interval from July 2011 to March 2023 (Figure 8). The analyses identified a phenomenon of soil subsidence that extended over an area of 28,388 km^2, as depicted by the black dashed line in Figure 7. This phenomenon was quantified by measuring its magnitude (see black observation points in Figure 7 with time series in Figure 8).

To ensure greater reliability of the analysis, only SAR pixels that presented temporal coherence greater than 0.7 were utilized in the analysis. This approach enabled PS-InSAR processing to achieve a quantity (density) of 110,000 points (13 points/ha) for PAZ (ascending and descending), 50,000 points (6 points/ha) for COSMO-SkyMed, and 25,000 points (3 points/ha) for Sentinel-1. The highest density of measurement points was observed on the PAZ satellite, which exhibited superior spatial resolution compared to the SAR images from COSMO-SkyMed and Sentinel-1.

PS-InSAR measurements were related to a reference point located in a common area in SAR images, which were assumed to be geologically stable and therefore not susceptible to soil subsidence processes (for location, see the lilac star in Figure 7). The results achieved an accuracy of approximately 0.6 mm for displacements and 0.5 mm/year for deformation velocity.

In Figure 7a–d, the maps with rates and spatial patterns of surface deformation of both satellite orbits, that is, ascending and descending can be observed. Displacements were measured along the LOS direction. In Figure 7e, the true displacement along the vertical component is observed from PAZ data (2019–2023). In all of these maps, negative values (yellow to red) represent movements away from the satellite (compatible with soil subsidence), while positive values (cyan to blue) represent movements toward the satellite (compatible with soil elevation). Furthermore, the similarity between the vertical maps and the LOS direction of the COSMO-SkyMed and Sentinel-1 satellites is observed.

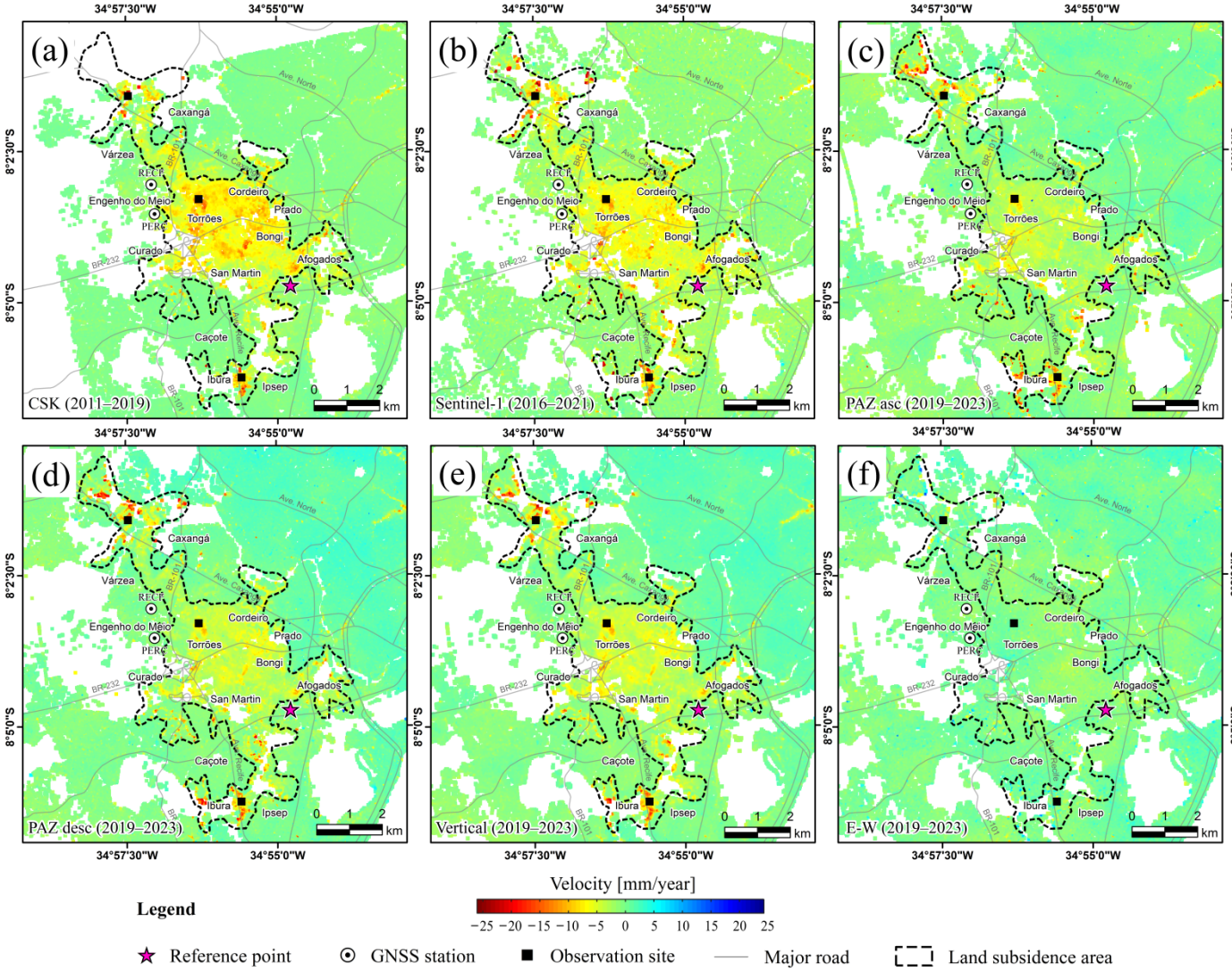

Figure 7. Velocity maps of the study area. (**a**) COSMO-SkyMed ascending, (**b**) Sentinel-1 descending, (**c**) PAZ ascending, and (**d**) PAZ descending show velocity measured along the satellite Line-Of-Sight (LOS) direction; (**e**,**f**) show velocity PAZ components computed along the vertical and east–west horizontal directions, respectively. The black dashed line represents the contour of the common area of land subsidence in SAR images. The black dots represent observation locations from the time series in Figure 8.

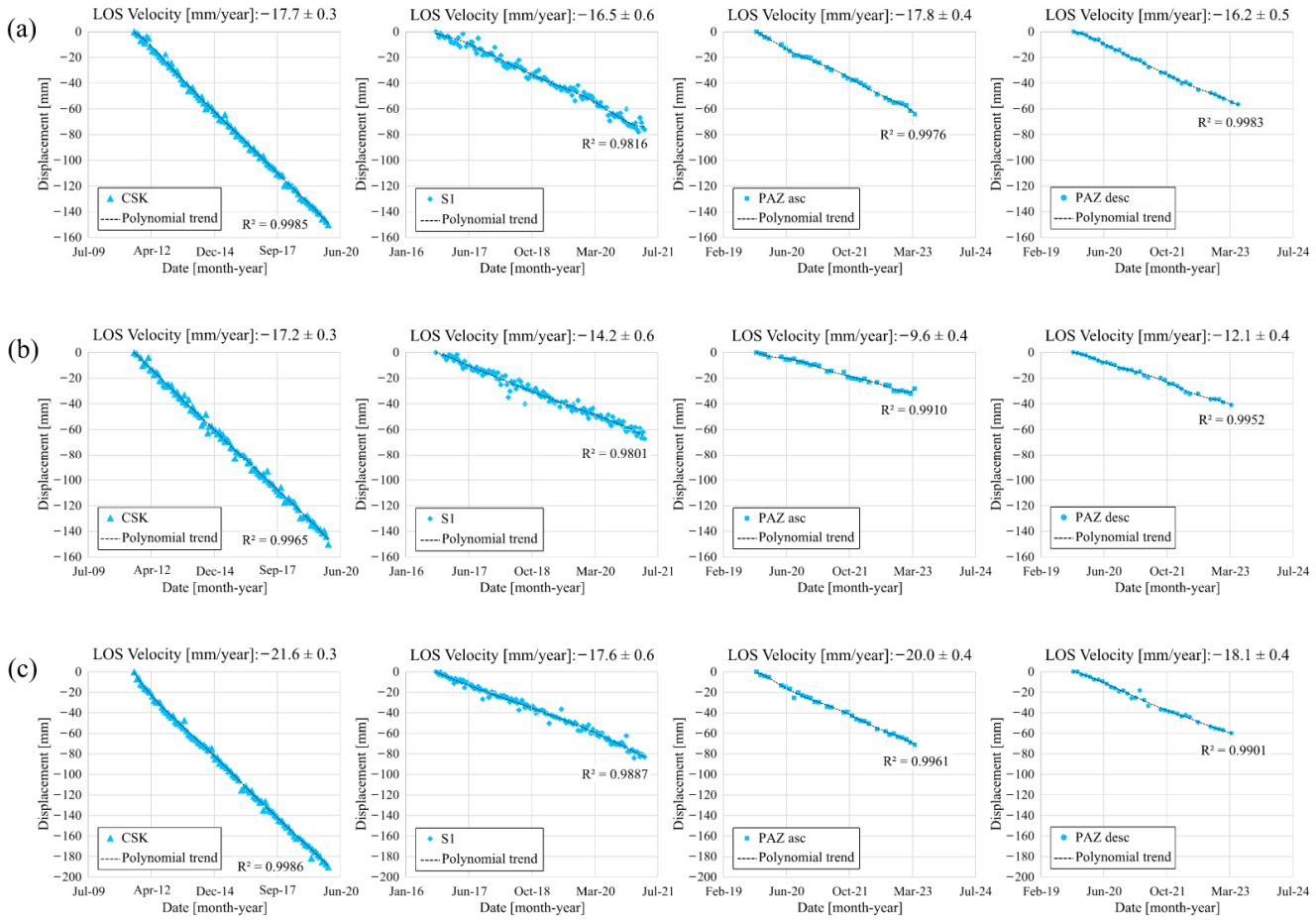

Figure 8. Average deformation time series covering the time interval of July 2011–March 2023. LOS velocity observations in the neighborhoods: (**a**) Várzea and Caxangá, (**b**) Torrões, and (**c**) Caçote, Ibura, and Ipsep.

In Figure 7f, surface movement is represented in the horizontal direction (E–W). The negative values (yellow to red) represent movements toward the west (left side), while the positive values (cyan to blue) represent movements toward the east (right side). Green pixels were considered to be stable, exhibiting velocities within the range of ±0.3 mm/year for COSMO-SkyMed, ±0.6 mm/year for Sentinel-1, and ±0.4 mm/year for PAZ (ascending and descending). In general, the horizontal displacement of the study area is practically stable, exhibiting slight movement in the west direction. The horizontal displacement exhibited a velocity of up to −7 mm/year. For the period from October 2019 to March 2023, the accumulated displacement to the west was approximately 20 mm.

The time series depicted in Figure 8a–c were derived from observation sites situated in the northern, central, and southern regions of the WZR (Figure 7), respectively. In Figure 8a, the observed LOS velocities were close to −20 mm/year throughout the Várzea and Caxangá neighborhoods. The accumulated settlement was approximately 210 mm for the period from 2011 to 2023. In Figure 8b, the LOS velocities were observed to be approximately −15 mm/year in the Torrões neighborhood. A similar value was also observed in the Engenho do Meio, Curado, San Martin, Cordeiro, Prado, and Afogados neighborhoods. The central part of the WZR exhibited the most extensive settlement area within the western region of the WZR. The accumulated displacement was approximately −175 mm for the period from 2011 to 2023. In Figure 8c, the lowest observed LOS velocity was −25 mm/year. The southern part of the WZR was the primary contributor to the city's most significant decline. The movement resulted in a displacement of approximately –260 mm over the period from 2011 to 2023. In general, the displacement rates of the

north, central, and south parts of the WZR were consistent with the velocity in the vertical direction (Figure 7e).

4.2. Land Cover Change Analysis

The urbanization analysis resulted in maps and graphs depicting the occupation process in the WZR for the period from 1950 to 2019 (Figures 9 and 10). The maps explored the north, central, and south parts of the region are represented, respectively, by Figure 9a–c. The study identified the widespread urbanization of the WZR throughout the second half of the 20th century, which represented the most significant anthropogenic impact on the region. This impact was greatest during the period depicted in Figure 10.

As illustrated in Figure 9a, urban expansion occurred along Caxangá Avenue and the Capibaribe River, accompanied by alterations to the watercourse (see Figure 3a). Additionally, residential and commercial properties were constructed as well as circulation roads. The process of urbanization intensified in the 2000s.

In Figure 9b, urban growth occurred along the BR-232 and BR-101 highways and Recife Avenue (see Figure 3b). In addition to the construction of residential and commercial properties, the implementation of the construction of circulation roads, hospitals (Pelópidas Silveira, and women's), public offices (Sudene, Chesf, Forum), and educational units (UFPE, IFPE, Military College) also occurred during this period. The process of urbanization intensified in the 1980s.

Figure 9c illustrates the expansion of urban areas along Recife Avenue (situated on the banks of the Tejipió River) close to the airport (see Figure 3c). This period saw the construction of lots for the development of residential and commercial properties, the construction of circulation roads, and the establishment of the Areais General Hospital and public body (EMLURB). The process of urbanization intensified once more in the 1990s.

Figure 10a illustrates the period of greatest population growth in Recife, which occurred between 1950 and 1970. This period saw an increase of 550,000 inhabitants, representing a growth of approximately 107% in the urban area. Over the past five decades, from 1970 to 2019, a similar population increase was observed, with a value of approximately 560,000 inhabitants, representing 52% growth.

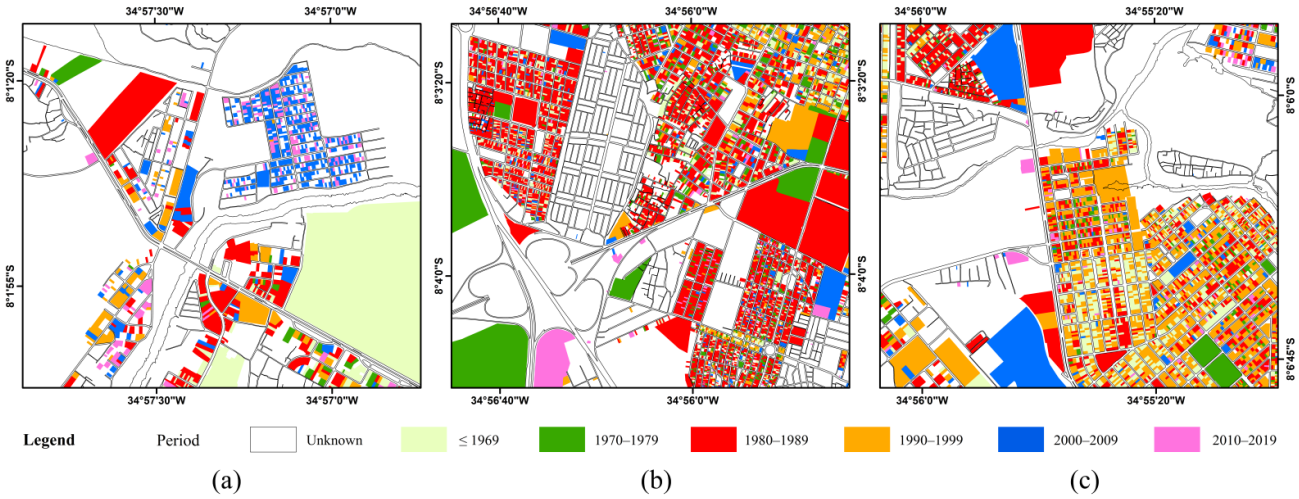

Figure 9. Evolution of urbanization in the west zone: (**a**) north, (**b**) center, and (**c**) south divisions.

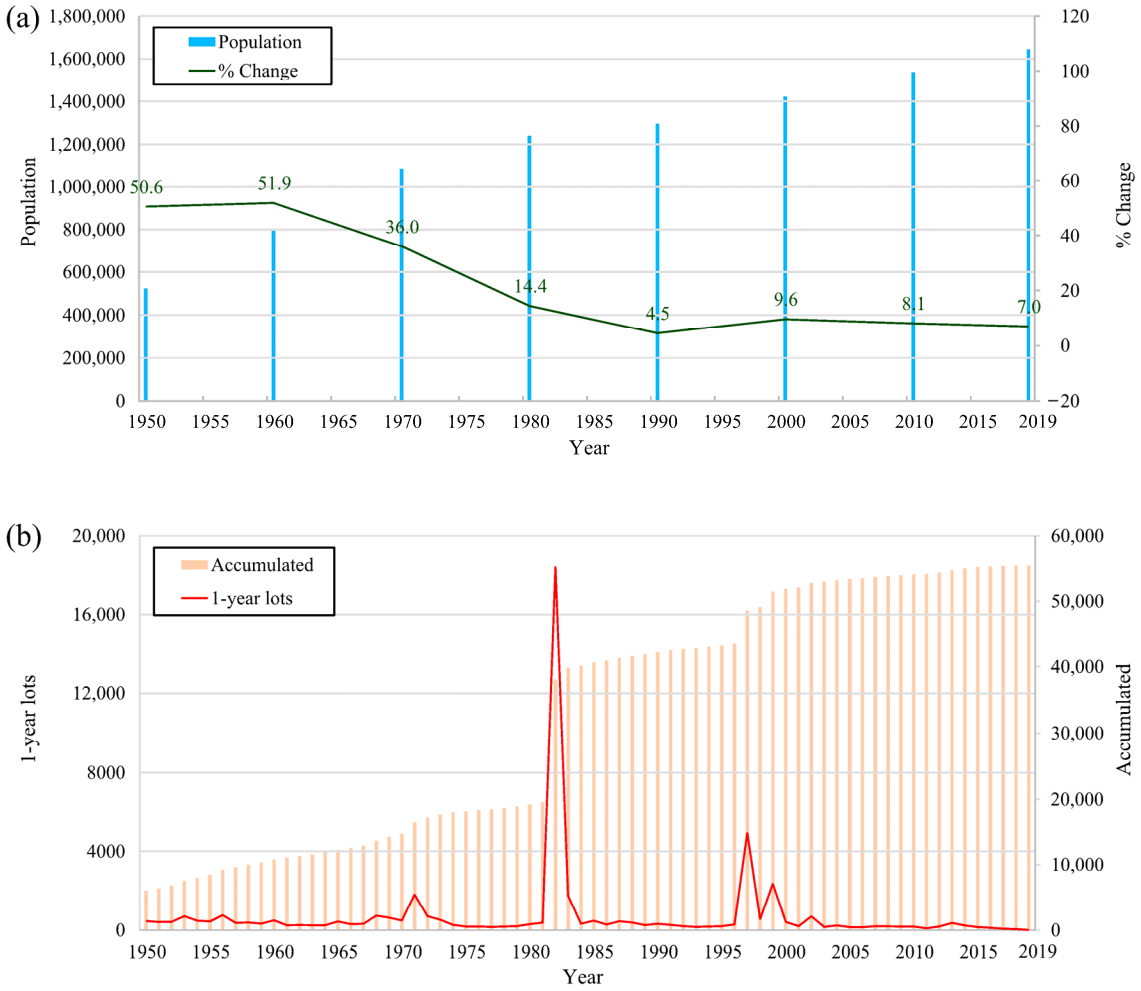

Figure 10. (**a**) Population growth in Recife. (**b**) Evolution of urban lots in the west zone.

Figure 10b illustrates the occurrence of three distinct periods of lot expansion in the WZR between the 1970s, 1980s, and 1990s. The smallest lot expansion was observed between 1970 and 1979, with a total of 4700 lots registered. The largest quantity was observed in the 1980s with a value of approximately 23,000 lots registered between 1980 and 1989. The year 1982 exhibited a particularly noteworthy value, with 18,500 lots registered. The value exhibited a 491% increase compared to the previous decade (1970) and a 58.8% reduction in relation to the subsequent decade (1990), with registration of 9500 lots for the period from 1990 to 1999.

4.3. Geotechnical Profiles Analysis

Figure 2 depicts the locations of the selected drilling sites in three different regions of the study area, as illustrated in Figure 11. The study analyzed six Standard Penetration Test (SPT) boreholes, with two in the northern part (SPT-1 and SPT-2, as shown in Figure 2a), two in the central part (SPT-3 and SPT-4, as shown in Figure 2b), and two in the southern part (SPT-5 and SPT-6, as shown in Figure 2c).

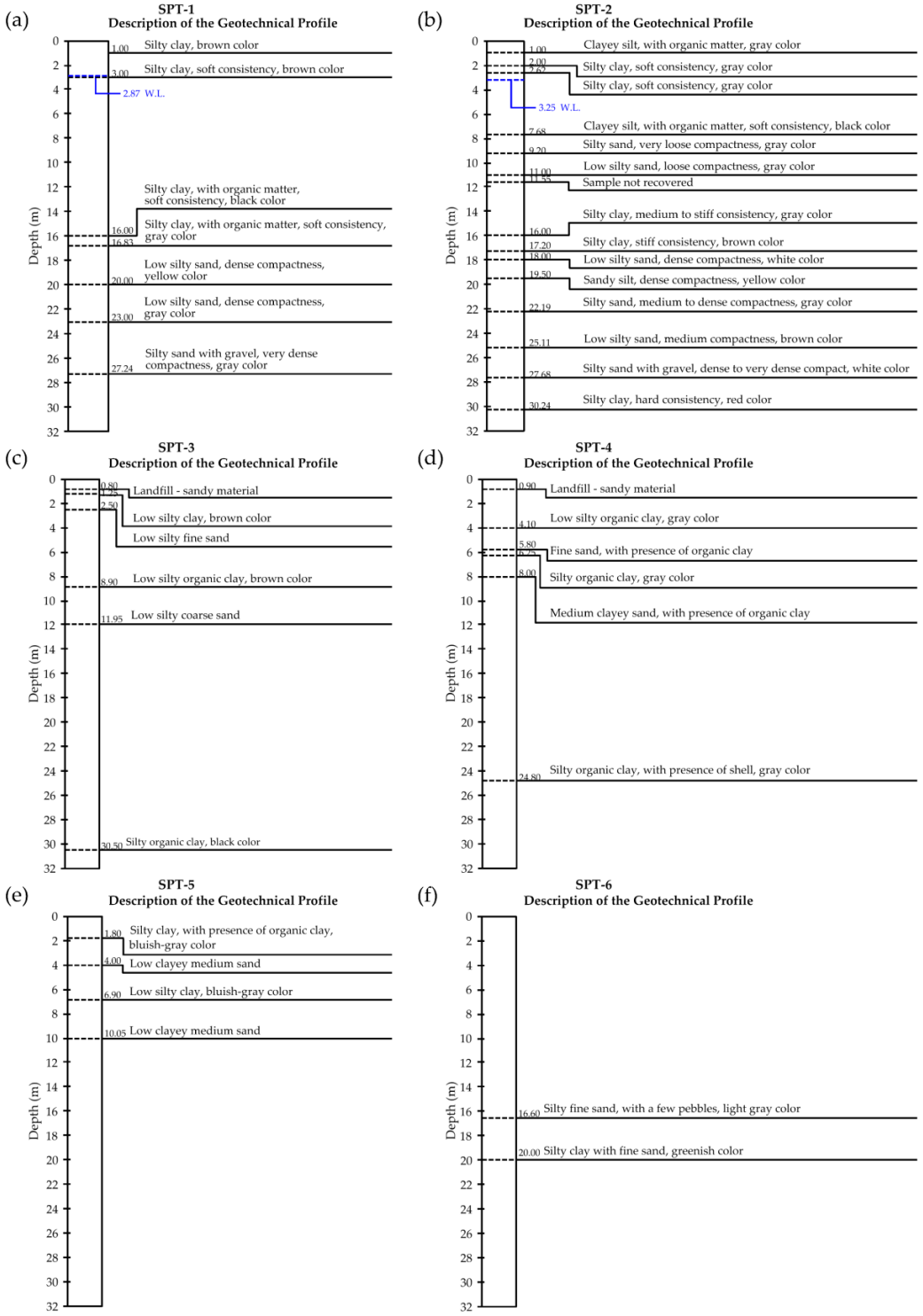

Figure 11. Description of Standard Penetration Test (SPT) profiles. Northern region: (**a**) SPT-1 and (**b**) SPT-2. Central region: (**c**) SPT-3 and (**d**) SPT-4. Southern region: (**e**) SPT-5 and (**f**) SPT-6.

Figure 11a,b presents the descriptions of the soil profiles of the northern part (Figure 2a), which reached depths of 27.24 m (SPT-1) and 30.24 m (SPT-2). In general, the first four layers of profiles 1 and 2 exhibit the presence of silty clay and/or clayey silt, which are soft in consistency and contain organic matter. In profile 1, these layers extended from a depth of 0 to 16.83 m, while in profile 2, they span from 0 to 7.68 m. From the fourth layer onward, sandy soils (e.g., silty sand and sandy silt) of medium to very compact classification are present.

Figure 11c,d illustrates the soil profiles of the central region (Figure 2b), which reached depths of 30.50 m (SPT-3) and 24.80 m (SPT-4). In the initial layer of both tests, the presence of a sandy landfill layer is evident, as this is a historically common practice in the Recife plain, aimed at reclaiming unfavorable lands. The intercalation of clay layers with sand layers was evidenced from the second layer. In the case of SPT-3, two thick organic clay layers of soft consistency were identified. The first of these was 6.40 m thick and was located between the depths of 2.50 m and 8.90 m. The second was 18.55 m thick and was located between the depths of 11.95 m and 30.50 m. In SPT-4, three organic clay layers of soft consistency were identified. The first layer was 3.20 m thick (between depths of 0.90 and 4.10 m), the second layer was 0.45 m (between depths of 5.80 m and 6.25 m), and the third layer was 16.80 m (between depths of 8.00 m and 24.80 m).

Figure 11e,f represents the descriptions of the SPT profiles of the southern region (Figure 2c), which reached depths of 10.05 m (SPT-5) and 20 m (SPT-6). In SPT-5, no evidence of a landfill layer was identified. The four layers identified are intercalated between silty clay and clayey sand. The two clay layers are 1.80 m and 3.15 m thick, respectively, and are located at depths between 0 and 1.80 m and between 6.90 and 10.05 m. In SPT-6, two layers were identified: the first, designated as silty fine sand with few gravels, is situated between 0 and 16.60 m, while the second, designated as silty sandy clay with fine sand, is located between 16.61 and 20 m depths.

4.4. GNSS Data Analysis

Monitoring at the RECF and PERC GNSS stations revealed the presence of movement in the WZR over the past 20 years (Figure 12). The stations exhibited similarities in terms of the displacement rates of the north, east, and vertical components. The RECF station was situated at UFPE and observations were made over the period from January 2003 to February 2018. The PERC station is situated at IFPE, at a distance of 875 m from the first initial geodetic structure. It has been operational since August 2018 until March 2022.

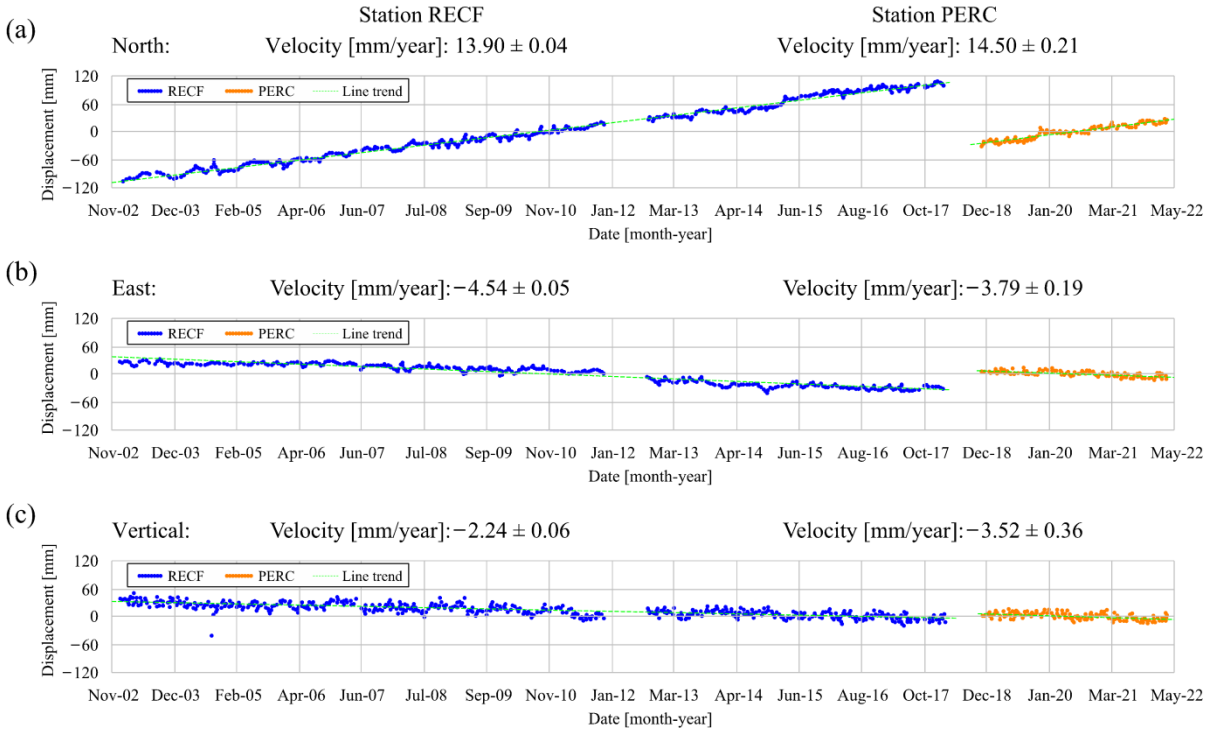

Figure 12. Positional monitoring of RECF and PERC GNSS stations. (**a**) North, (**b**) East, and (**c**) Vertical components.

Figure 12a illustrates the linear trend of the stations, which exhibited a positive northward movement. This component exhibited the highest velocity compared to the others. The highest value was observed in PERC with 14.50 mm/year, while in RECF it was 13.90 mm/year, both heading north. The difference between the seasons was the smallest in relation to the differences observed in the others, with 0.60 mm/year. For the period from January 2003 to August 2010 and from then until February 2017, the displacement in the RECF was approximately 110 mm in a southerly and northerly direction, respectively. For the period from August 2018 to July 2021 and from then until March 2022, the displacement in the PERC was close to 30 mm in a southerly and northerly direction, respectively.

Figure 12b illustrates a linear trend of the stations exhibiting a negative trajectory. The greatest rate of displacement rate was observed in RECF, with a value of −4.54 mm/year, while in PERC it was −3.79 mm/year, both in a westerly direction. The difference between seasons was 0.75 mm/year. The simultaneous displacements of the north (Figure 12a) and east (Figure 12b) components indicated horizontal movement to the northwest, with velocities of 14.62 mm/year and 14.99 mm/year for RECF and PERC, respectively. For the period from January 2003 to September 2010 and from then until February 2017, the displacement in RECF was approximately 40 mm in the east and 30 mm in the west, respectively. For the periods from August 2018 to May 2021 and from then until March 2022, the displacement in PERC was approximately 10 mm in the east and west, respectively.

Figure 12c illustrates the linear trend of the stations, which exhibited a negative trajectory in the vertical component. It exhibited the lowest displacement rate in comparison to the other two components. The highest velocity was observed in PERC with a rate of –3.52 mm/year, while in RECF it was −2.24 mm/year, both in a downward direction (compatible with soil subsidence). The seasonal variation exhibited the greatest discrepancy in comparison to the other observed variations, with a magnitude of 1.28 mm/year. For the periods spanning from January 2003 to June 2016 and from then until February 2017, the displacement in RECF exhibited a close to 35 mm upward movement and a 5 mm downward movement, respectively. For the periods from August 2018 to March 2021 and from then until March 2022, the displacement in PERC was approximately 5 mm in both an upward and downward direction.

The time series descriptions for the RECF and PERC stations (Figure 12a–c) indicated movements relative to the South American tectonic plate. After removing the displacement of the plate, the obtained values for the average north, east, and vertical velocities of the stations were determined to be 0.5 mm/year, −0.1 mm/year, and −2.1 mm/year for RECF and 1.0 mm/year, 1.1 mm/year, and −2.4 mm/year for PERC, respectively. These values represent the actual ground movement.

The residual velocities of the north, east, and vertical components for the RECF (2003–2018) station were projected into the LOS direction of the ascending COSMO-SkyMed (2011–2019) and descending Sentinel-1 (2016–2019) satellites. This resulted in an identical value of −1 mm/year. A similar analysis was conducted for the PERC (2018–2022) station, with the velocities in the north, east, and vertical components projected into the LOS direction of the ascending and descending orbits of the PAZ (2019–2023) satellite. The resulting values were −2 mm/year and −1 mm/year, respectively.

5. Discussion

5.1. Correlation between Subsidence Zones and Geotechnical Profiles

Figure 13 presents a comparison between the vertical PS-InSAR velocity (2019–2023) (Figure 7) and the locations of the SPT drilling sites that were previously analyzed in the three parts of the study area (Figure 2).

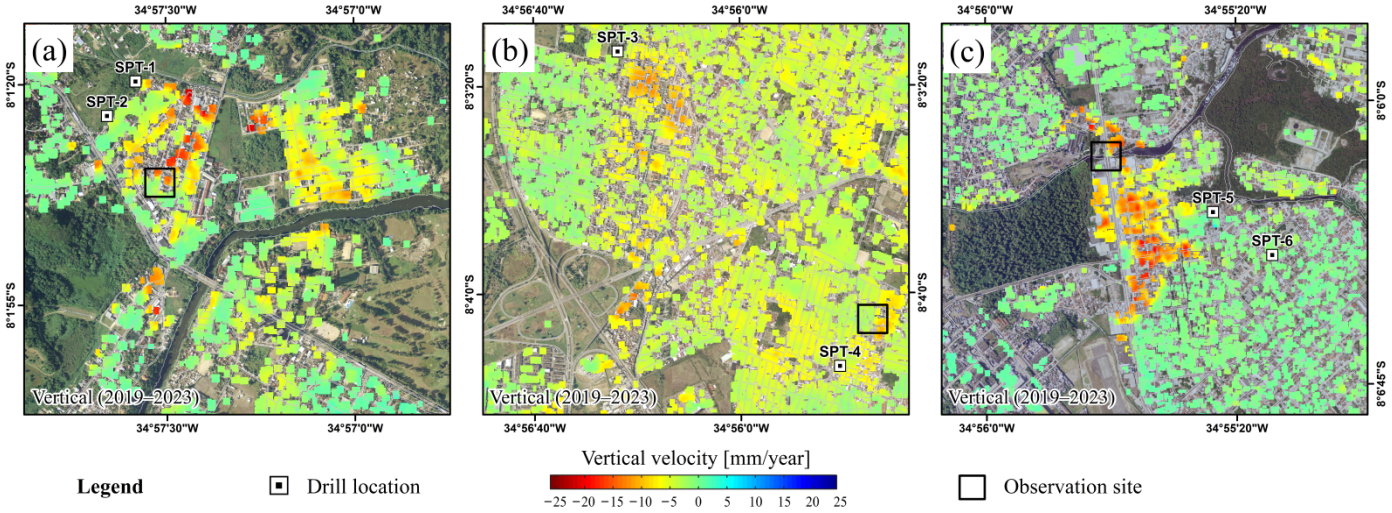

Figure 13. Land subsidence analysis detected by PS-InSAR (PAZ vertical 2019–2023) and SPT drill sites, parts of the western zone: (**a**) north, (**b**) center, and (**c**) south. The observation sites are shown in Figure 14.

It is essential to emphasize that the presence of compressible soil layers can provide compelling evidence of potential subsidence issues. Nevertheless, other geotechnical factors, such as the magnitude of building loads, the type of foundation design, which directly affects pressure distribution at different depths (pressure bulb), and the thickness of the compressible soil layer, among others, are crucial in determining the underlying causes of soil settlement.

From Figure 2a, which depicts the northern portion of Figure 13a, it can be inferred that the magnitude of the displacements observed in proximity to profiles 1 and 2 (Figures 11a and 11b, respectively) can be attributed to the presence of thick layers of soft organic clays. These soils exhibit highly compressible behavior and their occurrence is consistent with areas in proximity to watercourses.

In the central region (Figures 13b and 2b), profiles 3 and 4, as shown in Figures 11c and 11d, respectively, exhibit analogous behavior to those observed in the northern region. In these profiles, there are layers of soft organic clays with considerable thickness, which correspond to areas with higher-intensity displacements. This suggests that there is a probable correlation between subsidence and soils with high compressibility, as observed in the northern region.

In the southern region (Figures 13c and 3c), the clay layers of SPT-5 (Figure 11e) are observed to exhibit reduced thicknesses and lower compressibility compared to the profiles observed in the northern and central regions. Conversely, the clay layer in SPT-6 (Figure 11f) is situated at a greater depth (from 16 m on). The displacements recorded in the vicinity of SPT-5 (Figure 11e) and SPT-6 (Figure 11f) are of a smaller magnitude, which is consistent with the properties of the soils analyzed in these profiles. Moreover, SPT-5 is situated in a transition zone for displacements with greater magnitudes. In areas with more significant displacements, it is anticipated that the compressible soil layers will exhibit greater thicknesses than those identified in SPT-5.

To illustrate the impact of instability, buildings and infrastructures with different deformation rates were identified in the northern, central, and southern areas from the InSAR data. This was performed to conduct a technical field inspection to verify the presence of defects. The inspections were conducted in June 2024 (Figure 14).

A differential settlement occurs when portions of a structure deform unevenly. This phenomenon can be attributed to several factors, including variations in soil bearing capacity, uneven load distribution of loads on the foundation, fluctuations in soil moisture variations, construction errors, or the selection of an inappropriate foundation type.

In the northern area, a commercial warehouse for food distribution in the Caxangá neighborhood exhibited vertical displacement rates ranging from −0.8 mm/year to −15.3 mm/year.

As illustrated In Figure 14a, fissures and cracks extend from the interface between the prefabricated structural element and the masonry, propagating through the masonry wall and reaching the sidewalk pavement.

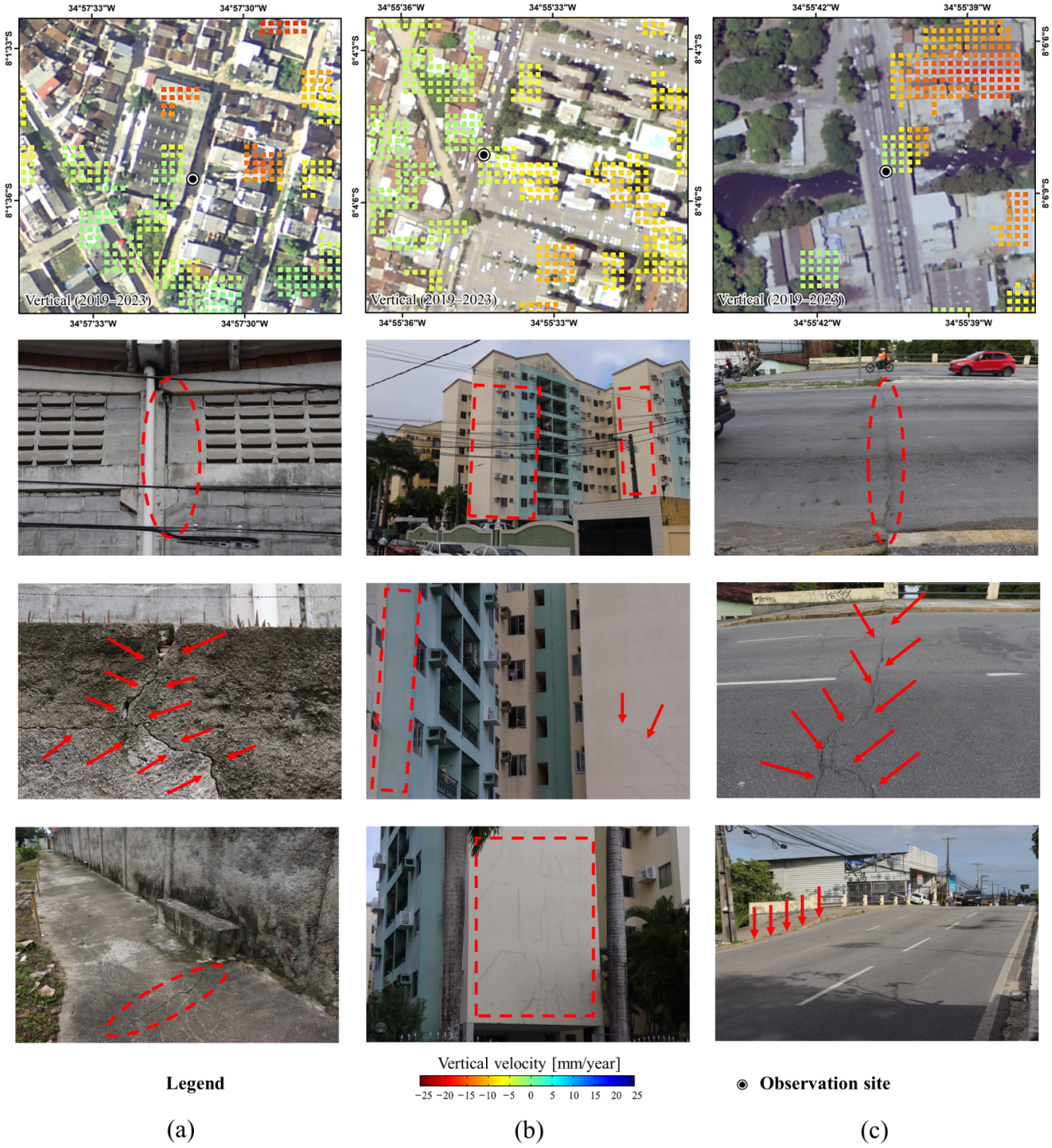

Figure 14. Effects of settlements on the structures in the areas under consideration: (**a**) north, (**b**) center, and (**c**) south.

In the central area, a residential condominium in the San Martin neighborhood had a tower exhibiting vertical displacement rates ranging from −2.6 mm/year to −9.4 mm/year. As illustrated in Figure 14b, fissures are visible throughout the facade of the building, resulting in damage to window frames and other facade elements.

In the southern area, a bridge spanning the Tejipió River on Recife Avenue, situated between the Ibura and Ipsep neighborhoods, exhibited vertical displacement rates that ranged from −1.7 mm/year to −8.3 mm/year. Figure 14c illustrates the presence of fissures and cracks at the interface between the bridge's superstructure and the avenue's pavement, thereby confirming the occurrence of differential settlements in the structure.

These examples illustrate the efficacy of employing InSAR as a continuous monitoring tool, offering a comprehensive detailed representation of deformations in expansive urban areas. This enables civil engineers and managers to make informed decisions, thereby facilitating the implementation of corrective and preventive actions in a more effective manner. Furthermore, the prompt identification of differential settlements allows for intervention before the damage becomes severe, thereby conserving resources and ensuring the safety of buildings and infrastructure.

5.2. Validation of the Results with GNSS Data and Previous Research in the WZR

Figure 15 presents a comparative analysis of the measured displacements and the monitoring of the RBMC stations utilized. One of the main advantages of the PS-InSAR time series analysis technique is that it provides a high degree of measurement density.

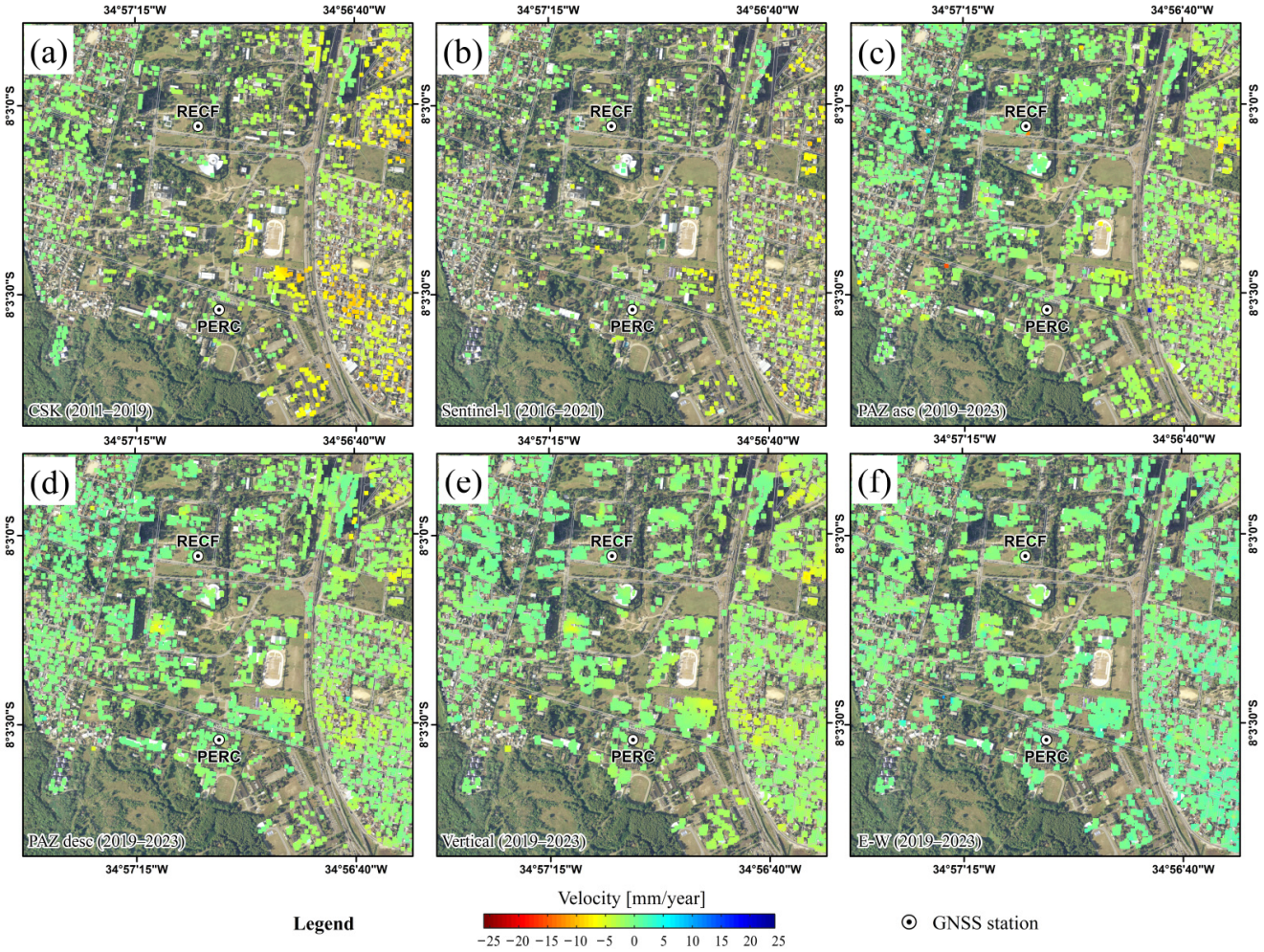

Figure 15. Deformation maps at RECF and PERC GNSS stations. (**a**–**d**) Show displacements measured along the satellite LOS direction for COSMO-SkyMed ascending, Sentinel-1 descending, PAZ ascending, and PAZ descending, respectively; (**e**,**f**) Show displacement components computed along the PAZ vertical and (E–W) horizontal directions, respectively.

This approach permitted the investigation of the large-scale spatial pattern of ground motion (see Figure 7), while GNSS provided a higher temporal resolution, which enabled the analysis of the dynamics of surface displacement (see Figure 12) [45].

To conduct a more comprehensive analysis of the results, in Figure 15, PS points exhibiting displacement rates proximate to those observed at the RECF and PERC GNSS stations were selected. The time series were derived by averaging the deformation measurements for each PS point.

The velocities of the PS points and GNSS stations were entered into Table 2 to compare ground deformation. The validation was based on an analysis of the movement rate derived from time series of LOS observations and displacements (vertical, E–W) from SAR data and multi-annual GNSS monitoring. This process permitted the assessment of ground displacement over the periods of coverage of the RBMC GNSS stations and SAR data. These datasets included RECF (2003–2018), PERC (2018–2022), COSMO-SkyMed (2011–2019), Sentinel-1 (2016–2021), and PAZ (2019–2023).

Table 2. Comparison between GNSS and PS-InSAR data.

Source	Velocity [mm/year]							Period
	North	East	Vertical	LOS CSK	LOS S1	LOS PAZ asc	LOS PAZ desc	
RECF	0.5	−0.1	−2.1	−1 *	−1 *	-	-	2003–2018
PERC	1.0	1.1	−2.4	-	-	−2 *	−1 *	2018–2022
CSK	-	-	-	−0.7 ± 0.3 **	-	-	-	2011–2019
S1	-	-	-	-	−0.8 ± 0.6 **	-	-	2016–2021
PAZ asc	-	-	-	-	-	0.9 ± 0.4 ***	-	2019–2023
PAZ desc	-	-	-	-	-	-	0.5 ± 0.4 ***	
Vertical	-	-	−0.4 ***	-	-	-	-	
E–W	-	0.9 ***	-	-	-	-	-	

Note: (*) Converted from north, east, and vertical components to LOS direction. (**) Regarding RECF. (***) Regarding PERC.

A comparison of the results of the GNSS stations and PS points in Table 2 revealed a high degree of similarity, with displacement values of less than 1 mm. The ground movement at the locations of the RECF and PERC GNSS stations exhibited minimal ground movement, indicating that the area is relatively stable for the use of permanent GNSS stations. The use of GNSS velocities (i.e., removing the tectonic component) can be employed to facilitate the referencing of InSAR velocities. For practical purposes, the use of InSAR components (vertical and east–west) can be useful for identifying tectonic plate displacement from long-term GNSS monitoring time series, in which Brazil is situated in the central portion of the South American tectonic plate [46].

5.3. Urbanization and Land Subsidence

The urban expansion of the WZR is a consequence of the process of interiorization of Recife. The region has a high rate of urbanization due to the presence of buildings and paved road systems, which have been constructed recently on unstable plains (estuarine areas, recovered areas) [18]. The anthropogenic action in the locality has caused several areas of soil subsidence due to the effect of ground compaction, which has been caused by the presence of acting loads [23]. The process is the result of the addition of permanent loads (landfills and construction elements) and movable loads (people and vehicles), which exert pressure on the surface and can take a long time, from several to many years, for the settlement of the soil material [47].

In this regard, the recent urbanization of the WZR, in conjunction with its geological condition, contributes to the process of soil subsidence. The region is characterized by mangrove sediments and alluvial and coastal deposits. The presence of compounds of clay, sand, and silt is prevalent in the area (Figure 11). The clay and silt units are distinguished

by high compressibility and act as a predisposing factor in soil subsidence induced by recent urbanization. In this regard, the region underwent profound transformations in its physiognomy and structure from the second half of the 20th century onward.

Over the decades from 1950 to 1970, a rapid population growth reached 550,000 inhabitants, equivalent to 107% growth (Figure 10a). It took almost 50 years, from 1970 to 2019, to achieve a similar increase, amounting to approximately 560,000 inhabitants. The considerable increase in the latter half of the 20th century contributed significantly to the greater implementation of lots in the region, particularly in the 1980s, with a value of approximately 23,000 lots. The greatest growth periods occurred approximately three times with intervals of 11 to 15 years (Figure 10b). The years with the highest growth were 1971 (1800 inhabitants), 1982 (18,500 inhabitants), and 1997 (4900 inhabitants). Consequently, the reduction in soil elevation resulting from recent urban expansion was considerable in several areas of the region (Figure 7), with the greatest impact observed in the north, central, and southwestern regions of the west zone (Figure 9).

As illustrated in Figure 9a, the urban expansion of the northern region was concentrated in the neighborhoods of Várzea and Caxangá. The construction activities were concentrated in the vicinity of the Capibaribe River and Caxangá Avenue. In Figure 13a, the rate of soil subsidence in the region ranged from a few millimeters per year to close to –20 mm/year (Figure 8a). A correlation was observed between the areas of intense subsidence (Figure 13a) and the most recent period of urbanization (Figure 9a), which occurred in the locality between 2000 and 2009. The greatest subsidence in the region is a consequence of the presence of extensive layers of soft organic clays present in the Capibaribe River plain (Figure 11a,b).

Figure 9b illustrates the urban evolution of the central part, which occurred along the neighborhoods of Torrões, Engenho do Meio, Curado, San Martin, Cordeiro, Prado, and Afogados. The construction activities were concentrated in proximity to the BR-232 and BR-101 highways, as well as Recife Avenue. In Figure 13b, the rate of soil subsidence in the region ranged from a few millimeters per year to approximately −15 mm/year (Figure 8b). This was characterized by the largest areas of subsidence in the west zone. Although the implementation of lots in Figure 9b is incomplete, it is possible to infer a correlation between areas of more intense subsidence (Figure 13b) and the period of greater urbanization (Figure 9b) for the interval from 1980 to 1989. The most significant deformations observed in the region reflect the presence of thick layers of soft organic clays (Figure 11c,d), which are similar to those observed in the north part.

Figure 9c illustrates the urban evolution of the southern part, which occurred in the neighborhoods of Caçote, Ibura, and Ipsep. The constructions took place along Recife Avenue and the Tejipió River. Figure 13c depicts the soil subsidence in the region, which ranged from a few millimeters per year to up to −25 mm/year (Figure 8a). This subsidence was characterized by the highest displacement rate in the west zone. A correlation was observed between the areas of intense subsidence (Figure 13c) and the most recent period of urbanization (Figure 9c), which occurred in the locality between 1990 and 1999. The greatest subsidence in the region under the effects of active loads may be due to thick layers of compressible soils near the Tejipió River (Figure 11e,f).

5.4. Geodetic Monitoring and Land Subsidence

The effect of soil subsidence in areas materialized by geodetic landmarks was observed in 10 stations (Figure 16). These included four benchmarks (BM) related to the IBGE high-precision altimetric network and six cadastral BM linked to the municipal cadastral reference network of the city hall from Recife. The investigation also analyzed horizontal movement.

As illustrated in Figure 16, the areas materialized by geodetic landmarks exhibited a range of subsidence rates and horizontal velocities (Table 3). The lowering rate ranged from a few millimeters per year to −20 mm/year, while the horizontal velocity ranged from a few millimeters per year to a maximum of close to −3 mm/year in a westward direction. These displacements have the potential to compromise the accuracy of BM and cadastral

stations in surveying the physical and geometric characteristics of the WZR, which is crucial for infrastructure design and management.

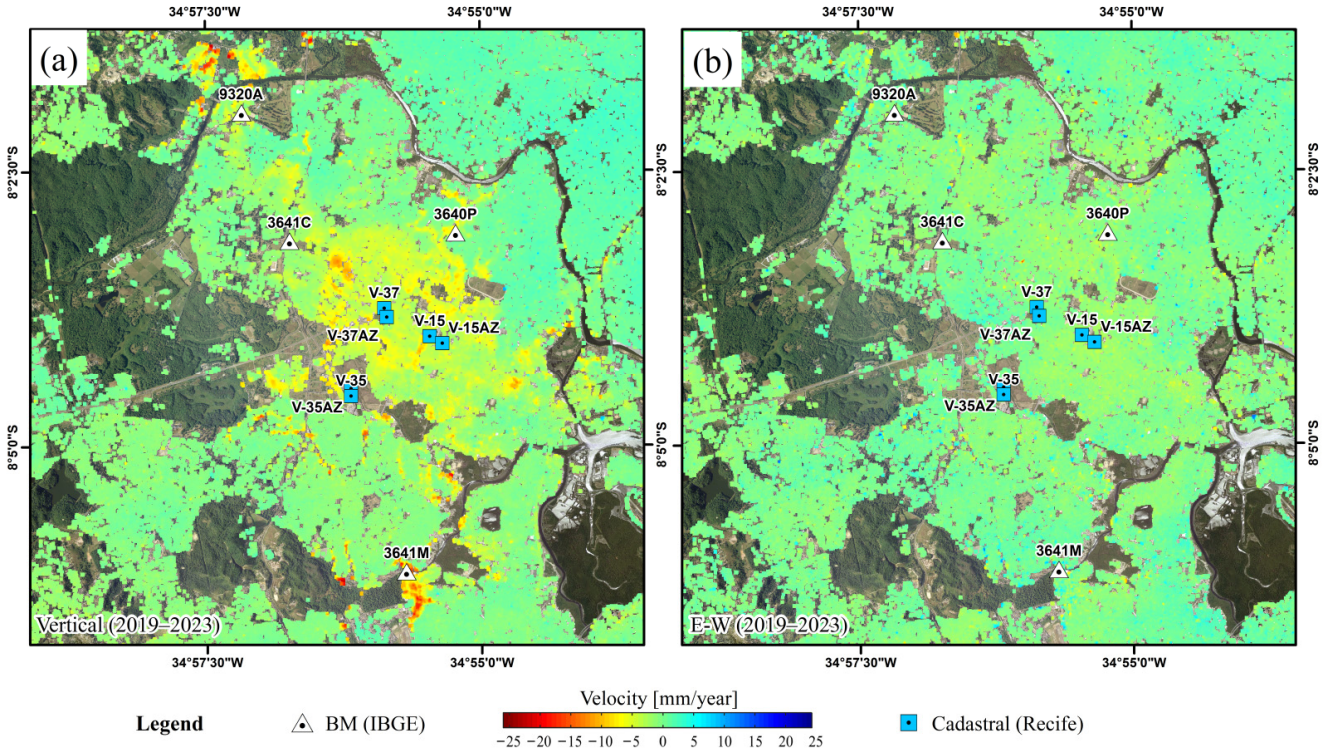

Figure 16. Geodetic benchmarks in surface movement areas from PAZ analysis 2019–2023: (**a**) vertical and (**b**) horizontal.

Table 3. Movement in BM and cadastral geodetic stations from PAZ analysis (2019–2023).

Code	Station	Agency	Updated	Vertical (mm/year)	E–W (mm/year)
9320A	BM	IBGE	2018	−3.5	0.3
3640P				−1.5	−2.5
3641C				−0.8	0.2
3641M			2021	−1.7	−2.2
V-15	Cadastral	Recife	2013	−6.1	−2.7
V-15AZ				−2.5	−1.9
V-37				−4.5	−0.2
V-37AZ				−3.6	−0.1
V-35				−3.9	−0.8
V-35AZ				−3.7	−1.0

Table 3 indicates that geodetic benchmarks materialized on land affected by soil subsidence require continuous updating of the coordinates. In particular, the horizontal component, which was the observable most impacted by the subsidence of the relief, requires the greatest degree of updating. The data from the last update showed greater outdatedness for registration stations, with surveys carried out in 2013 [48–55], while level references were readjusted in 2018 [56–60]. However, this process did not involve the measurement of elevation differences to calculate the altitude of the BM (Table 3). Rather, it involved the readjustment of the altimetric network with geopotential numbers to obtain altitudes with physical meaning.

Concerning geodetic benchmarks (Figure 16, Table 3), BM 3641M is situated in the main area of land subsidence in the west zone. For the period between 2011 and 2023, the accumulated settlement in the region results in a value close to 260 mm. According

to IBGE, the BM 3641M belongs to a line that forms circuits, whose closing errors do not meet high precision specifications. Therefore, the entity recommends caution when using the altimetric network. This indicates that the impact of subsidence in the station region is considerable.

5.5. Flooded Areas and Land Subsidence

Recife is one of the Brazilian capitals that is highly susceptible to flooding due to its geographical features. Several factors contribute to this vulnerability, including geology, geomorphology, pedogenetic conditions, climatic characteristics (especially rainfall distribution), tidal events, unplanned urbanization, informal occupations on reclaimed lands, and poor micro-drainage execution. As stated by Nobrega et al. [61], the combination of these factors results in a significant vulnerability to flood events in the city.

Based on the Drainage Master Plan's data, the city has 159 locations at a high risk of flooding [62]. In total, 9 out of these 159 locations are situated in the WZR area, which is affected by subsidence (Figure 17). Furthermore, 52% of the city's population resides in areas susceptible to flooding on rainy days. While 42% of the existing channels in the city remain in a natural state, the majority of them have been encroached upon by irregular constructions, with the banks of the channels themselves being affected as a result [63].

In May of 2022, heavy precipitation caused extreme floods in the eastern northeast region of Brazil, resulting in the tragic deaths of over 100 people. According to Zachariah et al. [64], these kinds of events are more likely to occur due to climate warming. To enhance resilience and effectively mitigate and adapt to the impact of climate-related disasters, Marengo et al. [65] and Nobrega et al. [61] have identified several actions that can be taken. These include improving early-warning systems, providing decision support for adaptation in climate-sensitive areas, and developing a strategic plan based on research and analysis.

The data presented in this work underscore the significance of incorporating considerations of soil displacements into the development of plans to mitigate flood hazards and construct resilient cities. This work also demonstrates the susceptibility of micro and macro-drainage solutions and urban infrastructure to the displacements presented in Table 3. These displacements vary from -3.5 mm/year to -6.1 mm/year (cumulative projection for the period from July 2011 to March 2023 varies from 41 mm to 72 mm).

These displacements can result in long-term alterations to the design conditions of micro-drainage systems. Furthermore, the displacements observed in BM and cadastral geodetic stations (discussed in previous sections) may lead to significant discrepancies in topographic surveys, which can have a considerable impact on the conveyance of the drainage system.

The preceding discussion has sought to demonstrate that SAR technology cannot be excluded from considerations about urban planning in a city with a comparable case study, irrespective of the purpose or phase of the study in question. The utility of SAR technology in this context is twofold. On the one hand, it facilitates the design of urban infrastructure. On the other, it permits the exploration of prospective scenarios under the influence of climate change.

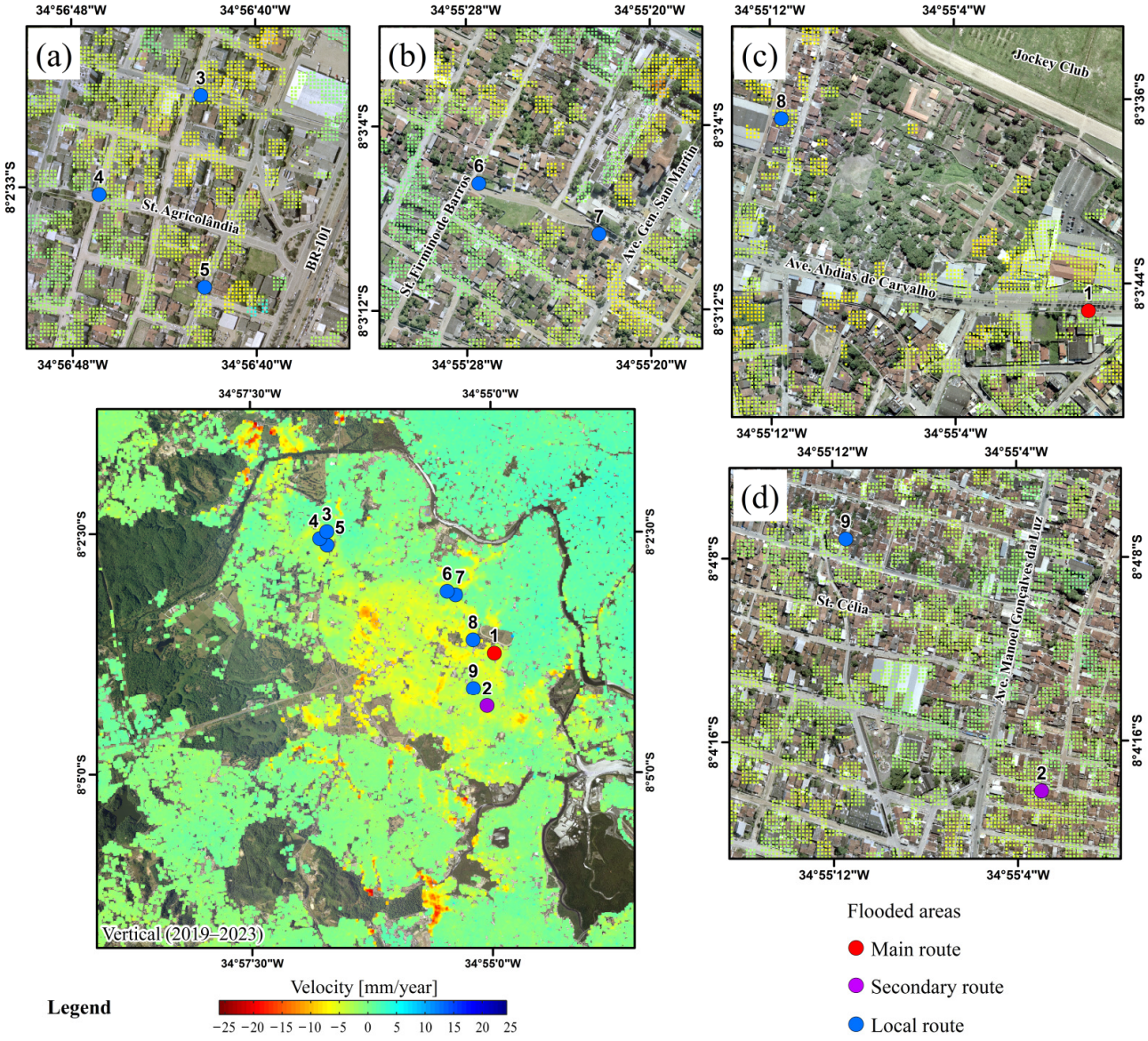

Figure 17. Flood areas affected by soil subsidence: (**a**) Várzea neighborhood, (**b**) Várzea and Cordeiro neighborhoods, (**c**) Prado neighborhood, and (**d**) Bongi and Mustardinha neighborhoods.

6. Conclusions

The analysis of soil subsidence in the WZR revealed that the region has experienced cases of subsidence induced by recent urbanization over the past 50 years. The phenomenon's development can be attributed to the addition of additional loads, such as landfills and constructions, in recent decades on unstable plain sites, including estuarine zones and reclaimed areas. The settlement process can take several years depending on the characteristics of the soil and the geology of the location.

The use of the PS-InSAR on COSMO-SkyMed, Sentinel-1, and PAZ SAR images acquired between July 2011 and March 2023 revealed the presence of several areas of ground subsidence. The most significant displacement rates were observed in the northern, central, and southern regions, with rates of up to −20 mm/year, −15 mm/year, and −25 mm/year, respectively. In these locations, coherence was observed between the measured displacements and the geological profiles of the analyzed soils, indicating a possible correlation. It can be concluded that

- The use of PAZ data acquired in ascending and descending orbits presents advantages in relation to the other SAR datasets used and acquired with only one orbit. It allows

for a greater understanding and perception of displacement by obtaining the vertical and E–W components;
- The combined analysis of InSAR images and continuous GNSS data presents relevant uses in the interpretation of displacement. This enables the identification of the spatial pattern and temporal dynamics of deformation;
- The GNSS data acquisition must be positioned over an area where there is greater ground movement, as determined by the PS-InSAR results. This is useful for analyzing the correlation with PS points;
- The West Zone of Recife is susceptible to subsidence due to its geotechnical characteristics and the presence of a thick soft-clay layer. However, other factors, such as the proper treatment (or absence) of the geotechnical foundations, control the settlement process and hence subsidence rates;
- It is crucial to consider soil subsidence when developing plans to mitigate flood hazards and build resilient cities;
- SAR technology is an invaluable tool in urban planning, regardless of the purpose or phase of the study. It is employed in the design of urban infrastructure and the prospecting of scenarios under climate change.

Future research will focus on employing InSAR technology for geotechnical monitoring in areas prone to slope instability and plains. This work will enhance methodologies for analyzing ground displacements and deformations, thereby contributing to risk management and safety in regions susceptible to landslides, subsidence, and other geotechnical instabilities.

Author Contributions: Conceptualization, W.d.O.S., L.G.d.M.R. and J.J.d.S.P.C.; data curation, W.d.O.S., L.G.d.M.R. and J.J.d.S.P.C.; formal analysis, W.d.O.S., L.G.d.M.R., A.M.R.-A. and A.d.P.P.; investigation, W.d.O.S., L.G.d.M.R., A.M.R.-A. and R.Q.C.; methodology, W.d.O.S., L.G.d.M.R., J.J.d.S.P.C., A.M.R.-A. and R.Q.C.; supervision, W.d.O.S., L.G.d.M.R., A.d.P.P. and W.R.A.J.; validation, W.d.O.S., L.G.d.M.R., A.M.R.-A. and W.R.A.J.; writing—original draft, W.d.O.S., L.G.d.M.R., J.J.d.S.P.C. and A.M.R.-A.; writing—review and editing, W.d.O.S. and A.M.R.-A. All authors have read and agreed to the published version of the manuscript.

Funding: The APC was funded by the University of Jaén (Spain).

Institutional Review Board Statement: Not applicable.

Informed Consent Statement: Not applicable.

Data Availability Statement: Most of the data used in this research is unavailable due to privacy restrictions. Sentinel-1 data used in this study are openly available at https://asf.alaska.edu/datasets/daac/sentinel-1/ (accessed on 4 June 2021).

Acknowledgments: The authors are thankful to Daniele Perissin for the free use of SARPROZ software. The Sentinel-1 data were provided by ESA, COSMO-SkyMed data were provided by ASI (Research project: 00020/8/783/1520), PAZ data were provided by INTA (Research projects: AO-001-039 and AO-003-037), and the geological map was provided by the Geological Survey of Brazil (CPRM) and DEM by Pernambuco Water and Climate Agency (APAC). Research was supported by POAIUJA 2023-24 and CEACTEMA from the University of Jaén (Spain) and the RNM-282 research group from the Junta de Andalucía (Spain).

Conflicts of Interest: The authors declare no conflicts of interest.

References

1. Abidin, H.Z.; Andreas, H.; Gumilar, I.; Brinkman, J.J. Study on the risk and impacts of land subsidence in Jakarta. *Proc. IAHS* **2015**, *372*, 115–120. [CrossRef]
2. Abidin, H.Z.; Andreas, H.; Gumilar, I.; Fukuda, Y.; Pohan, Y.E.; Deguchi, T. Land subsidence of Jakarta (Indonesia) and its relation with urban development. *Nat. Hazards* **2011**, *59*, 1753. [CrossRef]
3. UNESCO. *Guidebook to Studies of Land Subsidence Due to Ground-Water Withdrawal*; Prepared for the International Hydrological Programme, Working Group 8.4; Poland, J.F., Ed.; UNESCO: Paris, France, 1984.

4. Corapcioglu, M.Y. Land Subsidence—A. A State-of-the-Art Review. In *Fundamentals of Transport Phenomena in Porous Media*; Bear, J., Corapcioglu, M.Y., Eds.; Springer: Dordrecht, The Netherlands, 1984; pp. 369–444.
5. Cabral, J.; SANTOS, S.d.; Pontes Filho, I. Bombeamento intensivo de água subterrânea e riscos de subsidência do solo. *Rev. Bras. Recur. Hídricos* **2006**, *11*, 147–157.
6. Galloway, D.L.; Burbey, T.J. Review: Regional land subsidence accompanying groundwater extraction. *Hydrogeol. J.* **2011**, *19*, 1459–1486. [CrossRef]
7. Cigna, F.; Tapete, D. Present-day land subsidence rates, surface faulting hazard and risk in Mexico City with 2014–2020 Sentinel-1 IW InSAR. *Remote Sens. Environ.* **2021**, *253*, 112161. [CrossRef]
8. Abidin, H.Z.; Djaja, R.; Darmawan, D.; Hadi, S.; Akbar, A.; Rajiyowiryono, H.; Sudibyo, Y.; Meilano, I.; Kasuma, M.A.; Kahar, J.; et al. Land Subsidence of Jakarta (Indonesia) and its Geodetic Monitoring System. *Nat. Hazards* **2001**, *23*, 365–387. [CrossRef]
9. Ruiz-Armenteros, A.M.; Lazecky, M.; Ruiz-Constán, A.; Bakoň, M.; Delgado, J.M.; Sousa, J.J.; Galindo-Zaldívar, J.; de Galdeano, C.S.; Caro-Cuenca, M.; Martos-Rosillo, S.; et al. Monitoring continuous subsidence in the Costa del Sol (Málaga province, southern Spanish coast) using ERS-1/2, Envisat, and Sentinel-1A/B SAR interferometry. *Procedia Comput. Sci.* **2018**, *138*, 354–361. [CrossRef]
10. Cigna, F.; Osmanoğlu, B.; Cabral-Cano, E.; Dixon, T.H.; Ávila-Olivera, J.A.; Garduño-Monroy, V.H.; DeMets, C.; Wdowinski, S. Monitoring land subsidence and its induced geological hazard with Synthetic Aperture Radar Interferometry: A case study in Morelia, Mexico. *Remote Sens. Environ.* **2012**, *117*, 146–161. [CrossRef]
11. Stramondo, S.; Bozzano, F.; Marra, F.; Wegmuller, U.; Cinti, F.R.; Moro, M.; Saroli, M. Subsidence induced by urbanisation in the city of Rome detected by advanced InSAR technique and geotechnical investigations. *Remote Sens. Environ.* **2008**, *112*, 3160–3172. [CrossRef]
12. Ciampalini, A.; Solari, L.; Giannecchini, R.; Galanti, Y.; Moretti, S. Evaluation of subsidence induced by long-lasting buildings load using InSAR technique and geotechnical data: The case study of a Freight Terminal (Tuscany, Italy). *Int. J. Appl. Earth Obs. Geoinf.* **2019**, *82*, 101925. [CrossRef]
13. Xu, Y.-S.; Ma, L.; Du, Y.-J.; Shen, S.-L. Analysis of urbanisation-induced land subsidence in Shanghai. *Nat. Hazards* **2012**, *63*, 1255–1267. [CrossRef]
14. Chen, B.; Gong, H.; Li, X.; Lei, K.; Ke, Y.; Duan, G.; Zhou, C. Spatial correlation between land subsidence and urbanization in Beijing, China. *Nat. Hazards* **2015**, *75*, 2637–2652. [CrossRef]
15. Fryksten, J.; Nilfouroushan, F. Analysis of Clay-Induced Land Subsidence in Uppsala City Using Sentinel-1 SAR Data and Precise Leveling. *Remote Sens.* **2019**, *11*, 2764. [CrossRef]
16. Aljammaz, A.; Sultan, M.; Izadi, M.; Abotalib, A.Z.; Elhebiry, M.S.; Emil, M.K.; Abdelmohsen, K.; Saleh, M.; Becker, R. Land Subsidence Induced by Rapid Urbanization in Arid Environments: A Remote Sensing-Based Investigation. *Remote Sens.* **2021**, *13*, 1109. [CrossRef]
17. IBGE. População Residente. Available online: https://censo2022.ibge.gov.br/panorama/indicadores.html (accessed on 9 February 2024).
18. Cabral, J.J.S.P.; Farias, V.P.; Sobral, M.d.C.; de Paiva, A.L.R.; Santos, R.B. Groundwater management in Recife. *Water Int.* **2008**, *33*, 86–99. [CrossRef]
19. De Assunção Montenegro, A.A.; De Paiva, A.L.R.; Cavalcanti, G.L.; Da Silva Pereira Cabral, J.J.; Demetrio, J.G.A.; Montenegro, S.M.G.L. Águas subterrâneas na zona costeira da planície do Recife (PE): Evolução da salinização e perspectivas de gerenciamento. *Rev. Bras. Recur. Hídricos* **2009**, *14*, 81–93.
20. Santos, S.M. *Investigações Metodológicas Sobre o Monitoramento da Subsidência do Solo devido à Extração de Água Subterrânea—Caso da Região Metropolitana de Recife (English: Methodological Investigations about Landsubsidence Due to Groundwater Exploitation—Case of Metropolitan Region of Recife)*; Federal University of Pernambuco: Recife, Brazil, 2006.
21. Luna, R.M.R.; Garnés, S.J.d.A.; Cabral, J.J.d.S.P.; dos Santos, S.M. Groundwater overexploitation and soil subsidence monitoring on Recife plain (Brazil). *Nat. Hazards* **2017**, *86*, 1363–1376. [CrossRef]
22. Luna, R.M.R.; Garnés, S.J.d.A.; Cabral, J.J.d.S.P.; dos Santos, S.M. Suitability of GNSS for analysis of soil subsidence in Recife in a highly urbanized coastal area. *Nat. Hazards* **2021**, *106*, 1821–1837. [CrossRef]
23. Bedini, E. Persistent Scatterer Interferometry of Sentinel-1 time series to detect ground subsidence in the city of Recife, Brazil. *J. Hyperspectral Remote Sens.* **2020**, *10*, 1–9. [CrossRef]
24. IBGE. Cidades e Estados. Recife. Available online: https://www.ibge.gov.br/cidades-e-estados/pe/recife.html (accessed on 31 October 2022).
25. Melo, M.L. *Metropolitan Expansion and Underdevelopment: The Case of Recife*; UFPE: Recife, Brazil, 1978; p. 257.
26. Map. Available online: https://rigeo.cprm.gov.br/jspui/handle/doc/20596 (accessed on 12 December 2021).
27. Gusmão Filho, J.A. *Fundações do Conhecimento Geológico à Prática da Engenharia (In English: Foundations of Geological Knowledge to Engineering Practice)*; Editora Universitária UFPE: Recife, Brazil, 2002; p. 345.
28. Condepe. Orthophoto obtained from an aerial photogrammetric survey, 1974.
29. Google Earth Pro: Use of satellite imagery, USA, 2021.
30. Ferretti, A.; Prati, C.; Rocca, F. Permanent scatterers in SAR interferometry. *IEEE Trans. Geosci. Remote Sens.* **2001**, *39*, 8–20. [CrossRef]

31. Crosetto, M.; Monserrat, O.; Cuevas-González, M.; Devanthéry, N.; Crippa, B. Persistent Scatterer Interferometry: A review. *ISPRS J. Photogramm. Remote Sens.* **2016**, *115*, 78–89. [CrossRef]
32. Ruiz-Armenteros, A.M.; Lazecky, M.; Hlaváčová, I.; Bakoň, M.; Delgado, J.M.; Sousa, J.J.; Lamas-Fernández, F.; Marchamalo, M.; Caro-Cuenca, M.; Papco, J.; et al. Deformation monitoring of dam infrastructures via spaceborne MT-InSAR. The case of La Viñuela (Málaga, southern Spain). *Procedia Comput. Sci.* **2018**, *138*, 346–353. [CrossRef]
33. Fárová, K.; Jelének, J.; Kopačková-Strnadová, V.; Kycl, P. Comparing DInSAR and PSI Techniques Employed to Sentinel-1 Data to Monitor Highway Stability: A Case Study of a Massive Dobkovičky Landslide, Czech Republic. *Remote Sens.* **2019**, *11*, 2670. [CrossRef]
34. Perissin, D.; Wang, Z.; Wang, T. The SARPROZ InSAR tool for urban subsidence/manmade structure stability monitoring in China. In Proceedings of the 34th International Symposium for Remote Sensing of the Environment (ISRSE), Sydney, Australia, 10–15 April 2011.
35. Zebker, H.A.; Villasenor, J. Decorrelation in interferometric radar echoes. *IEEE Trans. Geosci. Remote Sens.* **1992**, *30*, 950–959. [CrossRef]
36. Pepe, A.; Calò, F. A Review of Interferometric Synthetic Aperture RADAR (InSAR) Multi-Track Approaches for the Retrieval of Earth's Surface Displacements. *Appl. Sci.* **2017**, *7*, 1264. [CrossRef]
37. Map. Lotes. Available online: http://dados.recife.pe.gov.br/pt_BR/dataset/area-urbana (accessed on 15 December 2021).
38. Coutinho, R.Q. *Estudo da Caracterização Geotécnica da Argila Orgânica do Recife*; Conselho Nacional de Desenvolvimento Científico e Tecnológico: Recife, Brasil, 1980.
39. Coutinho, R.Q. *Estudos Recentes da Caracterização Geológica-Geotécnica da Argila Orgânica do Recife*; Conselho Nacional de Desenvolvimento Científico e Tecnológico: Recife, Brasil, 2020.
40. IBGE. SIRGAS—Centro de Análise—IBGE. Downloads. Graficos. RECF. Available online: https://geoftp.ibge.gov.br/informacoes_sobre_posicionamento_geodesico/sirgas/graficos/RECF.png (accessed on 2 May 2022).
41. IBGE. SIRGAS—Centro de Análise—IBGE. Downloads. Graficos. PERC. Available online: https://geoftp.ibge.gov.br/informacoes_sobre_posicionamento_geodesico/sirgas/graficos/PERC.png (accessed on 2 May 2022).
42. IBGE. *Solução Multianual das Estações da Rede Brasileira de Monitoramento Contínuo dos Sistemas GNSS no Período de 2000 a 2019*; IBGE: Rio de Janeiro, Brazil, 2021; p. 117.
43. Santamaría-Gómez, A. SARI: Interactive GNSS position time series analysis software. *GPS Solut.* **2019**, *23*, 52. [CrossRef]
44. Hanssen, R.F. *Radar Interferometry: Data Interpretation and Error Analysis*; Kluwer Academic Publishers: Dordrecht, The Netherlands, 2001; Volume 2, p. 308.
45. Chen, Y.; Remy, D.; Froger, J.-L.; Peltier, A.; Villeneuve, N.; Darrozes, J.; Perfettini, H.; Bonvalot, S. Long-term ground displacement observations using InSAR and GNSS at Piton de la Fournaise volcano between 2009 and 2014. *Remote Sens. Environ.* **2017**, *194*, 230–247. [CrossRef]
46. Sánchez, L.; Drewes, H. Geodetic Monitoring of the Variable Surface Deformation in Latin America. In *Beyond 100: The Next Century in Geodesy*; Springer: Cham, Switzerland, 2023; pp. 197–208.
47. Waltham, T. *Foundations of Engineering Geology*, 3rd ed.; CRC Press: Boca Raton, FL, USA, 2009; p. 98.
48. Recife. Geodetic Station Monograph: V-15. Available online: https://esigportal2.recife.pe.gov.br/arcgis/rest/services/Planejamento/BASES_REDE_REFERENCIA_CADASTRAL/MapServer/0/15/attachments/33 (accessed on 4 June 2023).
49. Recife. Geodetic Station Monograph: V-15AZ. Available online: https://esigportal2.recife.pe.gov.br/arcgis/rest/services/Planejamento/BASES_REDE_REFERENCIA_CADASTRAL/MapServer/0/41/attachments/34 (accessed on 4 June 2023).
50. Recife. Geodetic Station Monograph: V-37. Available online: https://esigportal2.recife.pe.gov.br/arcgis/rest/services/Planejamento/BASES_REDE_REFERENCIA_CADASTRAL/MapServer/0/73/attachments/73 (accessed on 4 June 2023).
51. Recife. Geodetic Station Monograph: V-37AZ. Available online: https://esigportal2.recife.pe.gov.br/arcgis/rest/services/Planejamento/BASES_REDE_REFERENCIA_CADASTRAL/MapServer/0/74/attachments/74 (accessed on 4 June 2023).
52. Recife. Geodetic Station Monograph: V-35. Available online: https://esigportal2.recife.pe.gov.br/arcgis/rest/services/Planejamento/BASES_REDE_REFERENCIA_CADASTRAL/MapServer/0/69/attachments/69 (accessed on 4 June 2023).
53. Recife. Geodetic Station Monograph: V-35AZ. Available online: https://esigportal2.recife.pe.gov.br/arcgis/rest/services/Planejamento/BASES_REDE_REFERENCIA_CADASTRAL/MapServer/0/70/attachments/70 (accessed on 4 June 2023).
54. Recife. Geodetic Station Monograph: V08. Available online: https://esigportal2.recife.pe.gov.br/arcgis/rest/services/Planejamento/BASES_REDE_REFERENCIA_CADASTRAL/MapServer/0/8/attachments/20 (accessed on 4 June 2023).
55. Recife. Geodetic Station Monograph: AZ08. Available online: https://esigportal2.recife.pe.gov.br/arcgis/rest/services/Planejamento/BASES_REDE_REFERENCIA_CADASTRAL/MapServer/0/34/attachments/21 (accessed on 4 June 2023).
56. IBGE. Geodetic Station Monograph: 9320A. Available online: http://www.bdg.ibge.gov.br/bdg/pdf/relatorio.asp?L1=9320A (accessed on 4 June 2023).
57. IBGE. Geodetic Station Monograph: 3640P. Available online: http://www.bdg.ibge.gov.br/bdg/pdf/relatorio.asp?L1=3640P (accessed on 4 June 2023).
58. IBGE. Geodetic Station Monograph: 393Y. Available online: http://www.bdg.ibge.gov.br/bdg/pdf/relatorio.asp?L1=393Y (accessed on 4 June 2023).
59. IBGE. Geodetic Station Monograph: 3641C. Available online: http://www.bdg.ibge.gov.br/bdg/pdf/relatorio.asp?L1=3641C (accessed on 4 June 2023).

60. IBGE. Geodetic Station Monograph: 3640N. Available online: http://www.bdg.ibge.gov.br/bdg/pdf/relatorio.asp?L1=3640N (accessed on 4 June 2023).
61. Nóbrega, R.S.; Coutinho, C.D.; Lino, A.P.; de Albuquerque Wanderley, L.S. Flood Events in the City of Recife, Northeastern Brazil: History and Contemporary Risks. In *Urban Flooding in Brazil*; Mendonça, F., Farias, A., Buffon, E., Eds.; Springer International Publishing: Cham, Switzerland, 2023; pp. 171–192.
62. EMLURB. *Plano Diretor de Drenagem e Manejo das Águas Urbanas do Recife: Relatório do Diagnóstico do Sistema de Drenagem Existente*; EMLURB: Recife, Brazil, 2016; p. 333.
63. ICLEI. *Plano Local de Ação Climática da Cidade do Recife 2020*; ICLEI: São Paulo, Brazil, 2020; pp. 1–42.
64. Zachariah, M.; Junior, F.V.; Silva, T.; Santos, E.; Coelho, C.; Alves, L.; Martins, E.; Köberle, A.; Singh, R.; Vahlberg, M. *Climate Change Increased Heavy Rainfall, Hitting Vulnerable Communities in Eastern Northeast Brazil*; World Weather Attribution: London, UK, 2022; pp. 1–31.
65. Marengo, J.A.; Alcantara, E.; Cunha, A.P.; Seluchi, M.; Nobre, C.A.; Dolif, G.; Goncalves, D.; Assis Dias, M.; Cuartas, L.A.; Bender, F.; et al. Flash floods and landslides in the city of Recife, Northeast Brazil after heavy rain on May 25–28, 2022: Causes, impacts, and disaster preparedness. *Weather Clim. Extrem.* **2023**, *39*, 100545. [CrossRef]